
Article:
Davoodabadi, M. orcid.org/0000-0002-9868-5575, Liebscher, M., Sgarzi, M. et al. (5 more authors) (2022) Sulphuric acid sensing by single-walled carbon nanotubes incorporated alkali activated materials. Composites Part B: Engineering, 247. 110323. ISSN 1359-8368

https://doi.org/10.1016/j.compositesb.2022.110323

Sulphuric acid sensing by single-walled carbon nanotubes incorporated alkali activated materials

Maliheh Davoodabadi [a,b,c], ***Marco Liebscher*** [a,*], ***Massimo Sgarzi*** [b,c,*], ***Leif Riemenschneider*** [b,c], ***Daniel Wolf*** [d], ***Silke Hampel*** [d], ***Gianaurelio Cuniberti*** [b,c,e,f,*], ***Viktor Mechtcherine*** [a,*]

[a] *Institute of Construction Materials, Faculty of Civil Engineering, Dresden University of Technology, 01069 Dresden, Germany*

[b] *Institute of Materials Science and Max Bergmann Centre of Biomaterials, Faculty of Mechanical Science and Engineering, Dresden University of Technology, 01069 Dresden, Germany*

[c] *Dresden Centre for Nanoanalysis (DCN), Dresden University of Technology, 01069 Dresden, Germany*

[d] *Leibniz Institute for Solid State and Materials Research, 01069 Dresden, Germany*

[e] *Centre for Advancing Electronics Dresden (CfAED), Dresden University of Technology, 01069 Dresden, Germany*

[f] *Dresden Centre for Computational Materials Science (DCMS), Dresden University of Technology, 01069 Dresden, Germany*

* *M. Liebscher (marco.liebscher@tu-dresden.de), M. Sgarzi (massimo.sgarzi@tu-dresden.de), G. Cuniberti (gianaurelio.cuniberti@tu-dresden.de), V. Mechtcherine (viktor.mechtcherine@tu-dresden.de)*

Abstract

Concrete infrastructures are susceptible to corrosion in acidic environments; therefore, the constituent material should be engineered to sense the onset of ion penetration and propagation into the critical sites of the structure. Based on this concept, an intelligent alkali activated chemiresistor has been designed to sense the presence and concentration of sulphuric acid (H_2SO_4), considering the prerequisites of the structural health monitoring of durable cementitious structures. The proposed nanocomposite developed out of SWCNTs, fly ash, ground-granulated blast-furnace-slag (GGBS), and sodium silicate, is a built-in, low-powered, and ambience-operating structural element. H_2SO_4 was introduced on the surface of the highly alkaline, porous, and fractured sensor. The chemiresistor responses were distinguishable as the consequence of H_2SO_4 neutralization and speciation into sulphate (SO_4^{2-}) and hydrogen sulphate (HSO_4^-) species. This fundamental study can facilitate the future real-time aggressive ion interrogation potential of the SWCNT alkali activated nanocomposites in the construction industry.

Keywords

Chemiresistors; smart alkali activated nanocomposites; single-walled carbon nanotubes; conductive network; sensor microstructure; acid sensing; concrete corrosion.

1. Introduction

Sensors are intelligent functional materials with an aptitude to alter their normal characteristics in response to any ambient or desired introduced stimulus in the form of energy or matter. The outcome of those interactions should be a detectable signal. SWCNTs are one of these emerging sensors, which exhibit a tuneable electronic structure to be factionalized by elements, and a substantial surface area to be absorbed by stimulant substances. The sensing character of pristine SWCNTs (p-type) is mainly governed by the ballistic charge transport of the lattice holes located in the valence band of the carbons. Thus, an increase in the concentration of the hole carriers upon analyte exposure yields a rise in the conductance of the network [1–6]. SWCNT-based sensors can operate at ambient temperatures, and they are adaptable to sense a broad spectrum of analytes. Considering their mechanical and chemical resistance and resilience, they are multifunctional devices. Modified SWCNT-based devices can detect hazardous environmental contaminants on the scale of down to ultra-small in concentration (e.g., 0.010 ppt in [7]) and up to ultra-high in resolution (e.g., 0.370%·ppb^{-1} in [8]) [3,7–13]. Generally, the smart nanostructure of these sensing devices assists them to be sufficiently miniaturised, stable, sensitive and robust to be deployed for inspection and interrogation in operational sites with human-restricted access.

There are many hazardous and contaminated operational sites in the structure sector of the construction industry requiring real-time monitoring, namely, foundations, waste disposal systems, and marine or offshore infrastructures. They are remote and surrounded by aggressive acids, salts, and gases, causing severe damage to the structures, which are mainly constructed out of concrete. Because of the exposure to destructive environments, concrete experiences a deterioration of its constituent binder (cement) and loses functionality. The mentioned degradations are associated with the term "concrete corrosion" [14–17].

Concrete corrosion originating from sulphates (SO_4^{2-}) is one of the most prevalent concrete corrosion classes, since sulphates are naturally and abundantly available in the surrounding media or within the constituent raw material. Sulphate deterioration can occur because of chemical or biogenic reactions. In chemical corrosion, water influx into the concrete pore system introduces external SO_4^{2-} ions or liberates SO_4^{2-} from internal sources, which both result in the initiation of the material decomposition. However, in the biogenic class or "microbial induced concrete corrosion" (MICC), a chain of biological reactions driven by the metabolism of microorganisms produces gases and acids, particularly H_2SO_4 that eventually release SO_4^{2-} anions. The synchronous abovementioned intrusions, including the exposure to extreme acidic pH, lead to material destabilisation. Generally, corrosion is triggered by leaching of the cementitious framework and precipitation of weak and expansive monosulphoaluminate ($3CaO \cdot Al_2O_3 \cdot CaSO_4 \cdot 12H_2O$), ettringite ($3CaO \cdot Al_2O_3 \cdot 3CaSO_4 \cdot 32H_2O$), gypsum ($CaSO_4 \cdot 2H_2O$), and

thaumasite ($2CaSiO_3 \cdot CaSO_4 \cdot CaCO_3 \cdot 15H_2O$). The mechanism of sulphate corrosion and the damage imposed by H_2SO_4 are discussed intensively in the scientific community [16,18–25].

Many measures have been put forward for the modification of the cement to be more durable and resistant to corrosive conditions. Novel types of cements such as calcium aluminate or calcium sulphoaluminate, adding cementitious supplementary materials, and incorporation of heavy metals as antimicrobial agents are amongst the proposed solutions [16,17,26,27]. In parallel, alkali activated materials, especially modified geopolymers, have demonstrated the capability to withstand the chemicals and contaminants. The more stable geopolymeric framework and the absence of reactive portlandite ($Ca(OH)_2$) delay the dissolution of the microstructure and postpone the crystallisation of unfavourable aggregates [14,28,29].

Notwithstanding those countermeasures, monitoring should be done consistently and precisely to retain the integrity of the structures over their planned life span, as explained initially, by the sensors. Monitoring of concrete corrosion, hitherto, has been done by introducing external commercial sensors, mostly expensive and complicated, to measure the influencing parameters [30]. To achieve a higher degree of compatibility, certainty, and reliability, the sensors can be fabricated from the same or similar substances as the construction materials. This possibility results in a device, which may additionally be an integral load bearing and chemical resistant element, i.e., a multifunctional built-in sensor. According to the previous arguments, alkali activated materials have already displayed such features and recently applied for novel, unconventional applications. A sodium-based fly ash geopolymer coating was introduced for temperature and moisture sensing [31]. The developed sensor was additionally investigated for chloride-induced concrete corrosion [32]. Similarly, an automated deposition of sodium-based metakaolin geopolymers, 3D printed [33], and robot-sprayed [34], were used for temperature and strain sensing. Potassium-based fly ash geopolymers were developed as a capacitor for electrical energy storage and a piezoresistor for stress sensing [35]. Similar smart and multifunctional performances comparably have been reported for cementitious materials [36–41].

These innovative multifunctional sensors are electrolytic conductors, dependent on the pore solution content and charge balancing cations' degree of freedom for charge transport. To convert alkali activated materials to electronic conductors, SWCNTs can be embedded into their nano and microstructures. This involves the SWCNTs electronic network being fully generated and tightly percolated. So far, this strategy is not precisely applied to the alkali activated materials. However, an example of a similar approach can be the piezoresistivity study of reduced graphene oxide geopolymeric nanocomposites assessed by electrical impedance spectroscopy (EIS). The sodium-based fly ash geopolymer had an inherent ionic conductivity of 0.77 $S \cdot m^{-1}$ at 25 kHz and the 0.35 wt.% reduced graphene oxide nanocomposite exhibited an ionic plus electronic conductivity of 2.38 $S \cdot m^{-1}$ at 25 kHz. The nanocomposite accomplished tension and compression gauge factors of approximately double the composite, 20.70 and 43.87, respectively [42]. In

another relevant research, graphene was used as an electrode for an ionic conductor film made of sodium-based fly ash geopolymer for temperature and tensile strain sensing. The highest temperature sensitivity and gauge factor of the sensor, with an ionic conductivity of 1.72E-2 S·m^{-1} at 5 kHz, were 21.50 kΩ·°C^{-1} and 358, respectively [43].

The abovementioned horizons about SWCNT electronic sensors and alkali activated electrolytic sensors were the main reasons for initiating this research on the SWCNT alkali activated chemiresistors. Herein, a smart sodium-based fly-ash-GGBS alkali activated nanocomposite is introduced for $H_2SO_4/H_3O^+/SO_4^{2-}$ sensing regarding the sulphuric acid induced corrosion of concrete. To-date-reported sensors were validated by strain, temperature, moisture, and chloride ions, and a similar study of sulphuric acid sensing of SWCNTs embedded in alkali activated material was not found in the literature. The sensor can distinguish between the presence and concentration of sulphate anions and hydronium cations. It is a confined structural element, i.e., a built-in sensor, without the need for special architecture and substrate. Overall, the introduced sensor is comparatively multifunctional, sustainable, and discriminative, offering an operation in a very simplified and low-powered modality. Herein, the sensor fundamentals are elucidated and the conceptual design is presented. The nanostructure of the percolated network of SWCNTs in the alkali activated matrix is depicted by HRTEM for the first time. Furthermore, the nanocomposites' electrical properties, sensing behaviours, and microstructure are comprehensively characterised.

2. Materials and methods

2.1. Materials

The one-part blended alkali activated nanocomposites were fabricated by mixing nanofluids, and solid precursors and activator materials. The nanofluids were composed of conductive nanomaterial (SWCNTs), dispersant (sodium dodecylbenzenesulfonate (SDBS)), and ultrapure water as dispersion medium. SWCNTs, commercially known as TUBALL™, were provided from OCSIAL Europe, Leudelange, Luxembourg, and technical grade SDBS (MW 348.480 g·mol^{-1}) from Merck KGaA, Darmstadt, Germany. The ultrapure water (conductivity of 0.055 µS·cm^{-1}) was supplied from a dispenser device (Stakpure GmbH, Niederahr, Germany). Precursors were made of a combination of fly ash (Steament® H-4 FA) and ground granulated blast-furnace slag (GGBS), supplied from Steag Power Minerals GmbH, Dinslaken, Germany and Opterra GmbH, Leipzig, Germany, respectively. The activator was Sikalon® A (sodium disilicate powder) obtained from Wöllner GmbH, Ludwigshafen, Germany, with a molar ratio (SiO_2/Na_2O) of ≈2.1 and water content of ≈16 wt.%. The SWCNTs' specifications were elaborated in reference [44] and the chemical and physical properties of the precursors in reference [45].

2.2. Methods

2.2.1. Preparation

2.2.1.1. Nanofluids

Nanofluids were prepared according to the previously published papers on the synthesis of CNT alkali activated nanocomposites in the references [44,45]. In particular herein, the one-part methodology from the reference [44] was adapted. The modifications are described in the followings. SWCNTs were incorporated in the percentage of total nanocomposite oxides mass (wt.% of precursors plus activator oxides). The nanofluids and accordingly nanocomposites were fabricated with the SWCNT concentration of 0.100 wt.%, respecting the preliminary percolation study results. The mass and composition of nanofluids and nanocomposites were maintained constant in the total research.

The nanofluids were synthetised by dispersion of SWCNTs in SDBS [44,46,47] and ultrapure water with a Sonopuls HD 2200 ultrasonic homogenizer (Bandelin Electronic GmbH & Co. KG, Berlin, Germany) using a KE 76 probe. The ultrasonication was carried out for a total of 600 seconds per sample, applying a 50% cycle with 70% amplitude in a stepwise order, considering a total of 48 hrs intervening rest. Therefore, SWCNT, SDBS, and water were added into a glass vial and kept isolated in a fridge with a temperature of 1°C for 24 hrs. Afterwards, in-rest nanofluid was sonicated for 300 s and returned to the fridge for another 24 hrs. Finally, the second round of ultrasonication (300 s) was carried out, and the nanofluid was immediately shear-mixed with the solids. Therefore, SWCNTs obtained enough time to interact with SDBS, and be more efficiently individualised by the ultrasonication and shear mixer probe energies. The shear mixing of nanofluids and solid components was conducted for 600 s at 1000 rpm.

2.2.1.2. Nanocomposites

The nanocomposites were fabricated by casting shear-mixed nanofluids and solid components according to the reference [44] and cured in ambient environment conditions for 7 days and 28 days. The scheme of the synthesis process of the nanocomposites can be seen in the reference [44]. Before characterisation, the nanocomposites were heat treated for 24 hrs at 105°C in a Heraeus LUT 6050 drying oven (Kendro Laboratory Products GmbH, Langenselbold, Germany) to eliminate any potential residual entrapped water in the pore system of the nanocomposites. Regarding the results obtained in preliminary percolation study, the SWCNT alkali activated nanocomposites were percolated with the incorporation of 0.100 wt.% of SWCNTs, i.e., the SWCNTs' conductive network has been generated. Therefore, SWCNTs concentration of 0.100 wt.%, is considered for the chemiresistors fabrications and analysis in this research. The fabricated 7 and 28 days chemiresistors with 0.100 wt.% SWCNT incorporation accomplished rather similar mechanical performance because of the ambient curing methodology. The compressive and flexural strengths were 40±2.48 MPa and 7±0.21 MPa, respectively, measured

by Zwick 1445 universal testing system, ZwickRoell GmbH & Co. KG, Ulm, Germany.

2.2.1.3. Analytes

Sulphuric acid solutions in different concentrations and ultrapure water were utilised for the sensing experiments. The sulphuric acid stock solution (98% ACS reagent from Merck KGaA, Darmstadt, Germany) was diluted to reach the required concentration (calculated pH), 1.00E-05 mol·L^{-1} (4.70), 1.00E-03 mol·L^{-1} (2.73), 1.00E-01 mol·L^{-1} (0.97), and 1.00E+00 mol·L^{-1} (0.00). The SI unit of concentration "mol·L^{-1}" will be shown in a simple form of "M" in the rest of the manuscript. The specifications of sulphuric acid dilutions can be seen in Table 3 in the pH influence section. The pH of dilutions after preparation were measured by a VWR pHenomenal® pH 1100 L showing a ≤5% difference between calculated and measured values after equilibrium. For the sensing characterizations, 30 μL·(180 s)$^{-1}$ of the analyte was directly dropped on the marked centre-point of the back surface of specimens. The analyte was dropped by an Eppendorf Research adjustable volume pipette (10-100 μL) and the tip was renewed for each upcoming cycle.

2.2.2. Characterisations

2.2.2.1. Sensing and discriminating acquisition

The measurements were conducted by a laboratory-scale programmed sensing setup (Figure 1) according to the routine measurement procedures of the CNT-based sensing devices [8,13,48–51]. A KEYSIGHT B2912A Precision Source/Measure Unit (SMU) applied a 100 mV DC potential on the sensor electrodes (silver-coated parts of the nanocomposites) and accordingly captured the generated current. A Raspberry Pi computer board recorded the current at a frequency of 1 Hz and conveyed the data to a time-series database (InfluxDB) for visualization and further processing (Grafana). The received data in the form of the resistance, R, were converted to the resistivity/conductivity by applying the sensor geometry and normalized by means of relative resistance in percentage, i.e., $100 \cdot \left((R_1 - R_0) \cdot R_0^{-1}\right)$, for the sensing analyses. The prism sensor and sensing geometries were 60×10×10 mm^3, and 40×10×10 mm^3, respectively. This means, all surfaces at both ends of the prism were covered by silver paint in a 10 mm length across the edges to yield built-in electrodes. To calculate the standard error for each point of the data (shown by grey highlights around the sensing curves), the measurements were repeated on three pieces of newly-produced set of individual specimens.

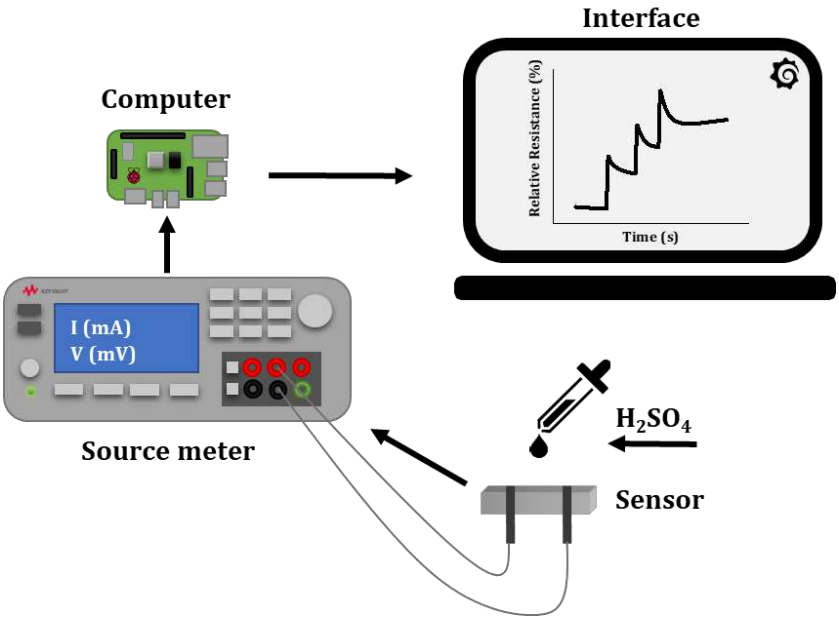

Figure 1. The laboratory-scale programmed sensing setup.

2.2.2.2. Transmission electron microscopy (TEM)

In order to visualize the network of individual SWCNTs within the blended alkali activated nanocomposite matrix, high-resolution transmission electron microscopy (HRTEM) was performed on an FEI Tecnai F30 (ThermoFisher Scientific company). This instrument was operated at a 300 kV acceleration voltage, providing a point resolution of 0.19 nm. Since HRTEM requires electron-transparent specimens with thicknesses of a few tens of nanometre, a TEM lamella was prepared by Focussed ion beam (FIB) using an FEI Helios 5 CX, ThermoFisher Scientific company. To this end, a cleaved piece of specimen was embedded in a mixture of G1 epoxy resin and carbon nanoparticles, to improve the material ductility and conductivity for FIB cuttings. The reinforced specimen was kept in vacuum condition for 24 hrs. Subsequently, the specimen was mounted on a stub, and ground by diamond foil and tripod polisher to a thickness of ≈1 μm. The sample was cleaned several times in an ultrasonic bath between these steps. The entire process was repeated several times until all surfaces and pores of the nanocomposite were infiltrated by the epoxy resin. Next, some layers of platinum were deposited on the specimen to protect the surface from beam damage during cutting a cross-section using the FIB. In the final stage, a lamella was cut by the FIB and fixed on a Mo TEM omniprobe lift-out grid (Figure 2).

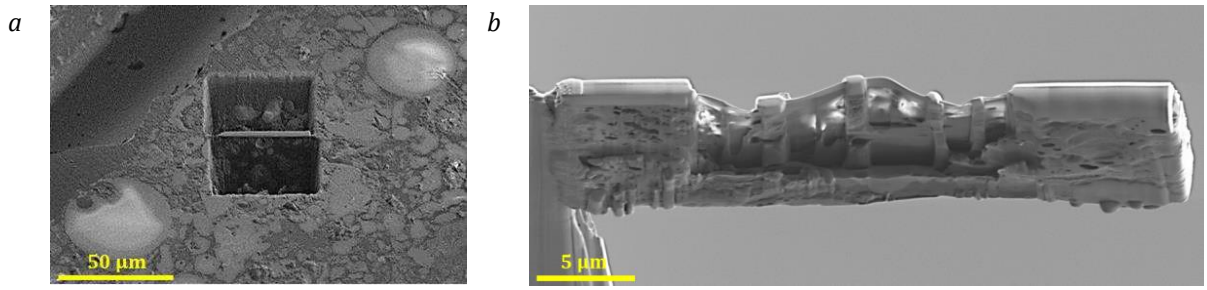

Figure 2. The TEM specimen prepared by epoxy embedding and FIB cutting; a- SEM image of platinum

covered cross-section; b- SEM image of the TEM-lamella.

2.2.2.3. Scanning electron microscopy (SEM)

SEM was performed by a GeminiSEM 500 (Carl Zeiss QEC GmbH, Jena, Germany) in a high vacuum condition (≈ 10^{-5} mbar) and at a landing energy (also EHT) of 3.00 kV on the surface and ruptured cross-sections of the specimens. The specimens were kept in vacuum condition 24 hrs before the microscopy without doing any additional treatment.

2.2.2.4. Fourier-transform infrared spectroscopy (FTIR)

FTIR was done by a Bruker FTIR spectrometer Vertex 80v (Bruker Optics GmbH & Co. KG, Germany) with a Globar radiation source, KBr beam splitter, and DTGS detector. The measurement resolution was 4 cm^{-1} from 400 to 4000 cm^{-1} at the ambient laboratory conditions. The samples were prepared by the KBr pellet method. The KBr powder (200 mg) was mixed with the nanocomposite powder (10 mg) and pressed for 120 s at 7 tonnes by using a hydraulic press. The nanocomposite powder was obtained by scraping the sulphuric acid exposed (1.00E-01 M) and the non-exposed surface of the specimens with a scalpel.

2.2.2.5. Mercury intrusion porosimetry (MIP) and roughness measurements

The porosity of the nanocomposites was measured by Porotec mercury intrusion porosimeters, Pascal 140, and Pascal 440 to obtain broad span spectra. The measurements were conducted on cubes of the nanocomposites with a ≈10 mm edge. Roughness, scan resolution of $0.\overline{33}$ µm, was evaluated by a Bruker stylus profilometer, Dektak XTL™ on the untreated full-size samples.

2.2.2.6. pH measurements

As mentioned in section 2.2.1.3. Analyte, pH values were measured by a VWR pHenomenal® pH 1100 L. Before any pH recording, the probe was washed with ultrapure water and calibrated afterwards. For the simulation of the pH variation of sulphuric acid solutions after contact with the nanocomposite, 6 mL of 1.00E-01 M (pH 0.97) sulphuric acid was diluted with 9 mL of ultrapure water, hence reaching a hydronium concentration of 5.45E-02 M and pH of 1.21. Subsequently, a piece of nanocomposite (ca. 7850 mg) was broken into coarse-grained particles and added to the sulphuric acid diluted solution.

3. Results and discussion

3.1. Electrical properties

The measured resistance of percolated alkali activated nanocomposites with incorporation of 0.100 $wt.\%$ of SWCNT are approximately 90 Ω and 70 Ω respectively for 7-day

and 28-day nanocomposites. These magnitudes of electrical resistance, considering the geometry of nanocomposites (60×10×10 mm^3), grant the 7-day and 28-day nanocomposites a resistivity of 0.22 Ω.m and 0.18 Ω.m, and correspondingly a conductivity of 4.80 $S.m^{-1}$ and 6.02 $S.m^{-1}$ (Table 1). Table 1 shows the electrical properties of nanocomposites are age-dependent and vary over the curing period. The higher conductivity of 28-day nanocomposites (approximately 25% higher) can be attributed to a more developed nano-framework of the matrix causing SWCNTs to generate a rigid and compressed conductive network. The observed trend, furthermore, is consolidated with another study of SWCNT incorporation (the same nano-additive product from OCSIAL) in the cementitious nanocomposites [52]. Compared to the similar alkali activated nanocomposites, lower magnitudes of conductivity were reported for those incorporating higher quantities of CNT. Selected examples are summarized in Table 2, for comparison. The applied CNT nano-electrical structures (chirality) and the status of CNTs' dispersion and distribution have the most significant effects on the reported differences in the nanocomposites' electrical properties. In addition, operational parameters such as fabrication and curing methodologies might be influential, however to a lower degree.

Table 1. Electrical properties of SWCNT alkali activated nanocomposites (specimen geometry: 60×10×10 mm^3; SWCNT conc. 0.100 wt.%).

Property	Symbol	Unit	7-day	28-day
Resistance	R	Ω	88.33 ± 6.17	70.32± 4.23
Resistivity	ρ	$\Omega \cdot m$	0.22 ± 0.02	0.18 ± 0.01
Conductivity	$\kappa\ (\sigma)$	$S \cdot m^{-1}$	4.83 ± 0.32	6.02 ± 0.39

Table 2. Reported conductivities of alkali activated nanocomposites.

Reference	Matrix material	Conductive additive	Concentration ($wt.\%$)	Conductivity ($S \cdot m^{-1}$)	Ref conductivity ($S \cdot m^{-1}$)
[53]	Clay	SWCNT	0.20	1.90E-03	9.80E-04
[54]	Slag	MWCNT	2.50	45E-03	15E-03
[55]	Fly ash	MWCNT	1.00	3.00	1.50

3.2. Morphology of the SWCNTs' network

The spatial distribution of SWCNTs in the matrix microstructure is displayed in Figure 3 and the areas with the high content of SWCNTs are indicated by the yellow dashed boxes. The modified ultrasonication and shear mixing could detangle SWCNTs' bundles to a much higher degree compared to the previous practices of CNT incorporations into the identical two-part and one-part alkali activated matrices [44,45]. This inner-matrix distribution of SWCNTs was the prerequisite for nanocomposites percolated character and obtained conductivities in Table 1. Considering the bulk mass of the nanocomposites, a significant localization or segregation of CNTs

is not observed, and SWCNTs have a random and stochastic fractal distribution pattern through all the entire mass of the alkali activated material, highlighted by the yellow dashed boxes in Figure 3. The localized or segregated networks are mostly common in polymeric nanocomposites, where CNTs are distributed in one phase of the blend or at the interface of copolymers [56].

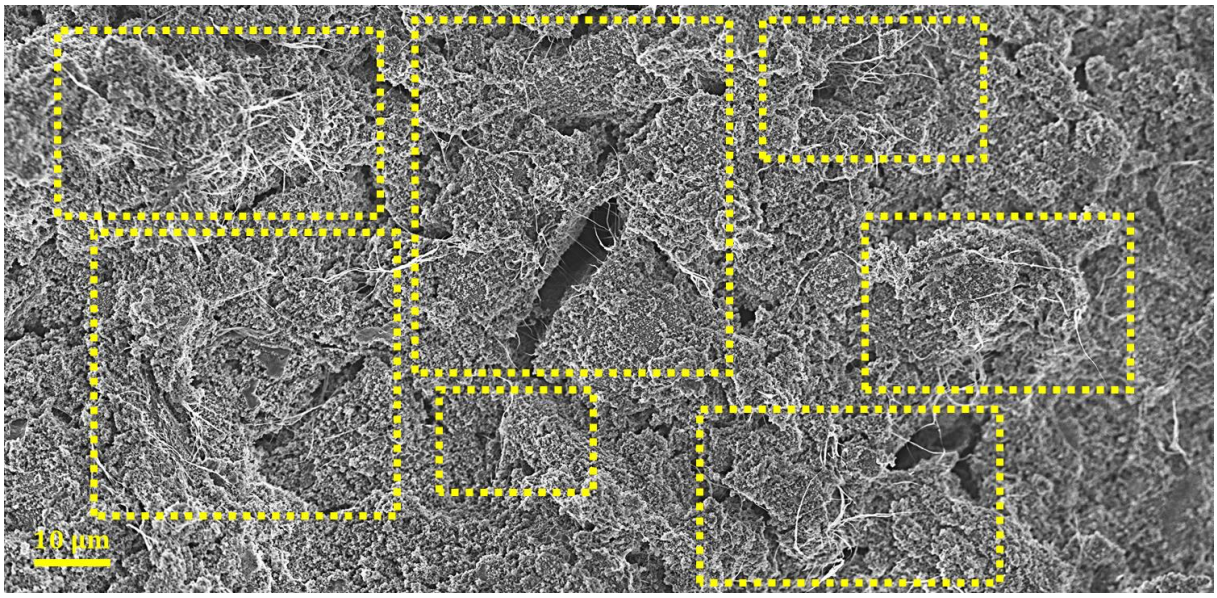

Figure 3. The spatial morphology and distribution of SWCNTs (conc. 0.100 wt.%) in the intentionally fractured inner-matrix cross-section.

The percolated conductive network of embedded SWCNTs in the alkali activated matrix is imaged with the atomic-scale HRTEM and depicted in Figure 4. The observed parallel patterns with approximately 16 Å spacing are the SWCNTs' nanostructures (adjacent tubes/shells). The well-distributed SWCNTs (shown in Figure 3) have established a dense interconnected grid made of thick agglomerations spreading in all directions of the matrix. This state of SWCNTs' connection is attributed to the percolated conductive network, which is highlighted in Figure 4 by the yellow dashed continuous pathways. These continuous distributions and pathways of SWCNTs in the matrix nanostructure are the main reasons of observed nanocomposites' low resistivity or high conductivity.

Such SWCNTs' intra-network configurations and layouts are shown with more detail in Figure 5. According to these HRTEM micrographs, SWCNTs-nanostructures are constituted out of at least ≈10 individual shells, which construct many alignments and conjunctions as depicted in Figure 5 a, and magnified in Figure 5 b. These dense nanostructures are composed of SWCNTs' crosslines (yellow dashed pathways in Figure 5 c), or perpendicular and horizontal orientations of SWCNTs (yellow dashed circle and box in Figure 5 d).

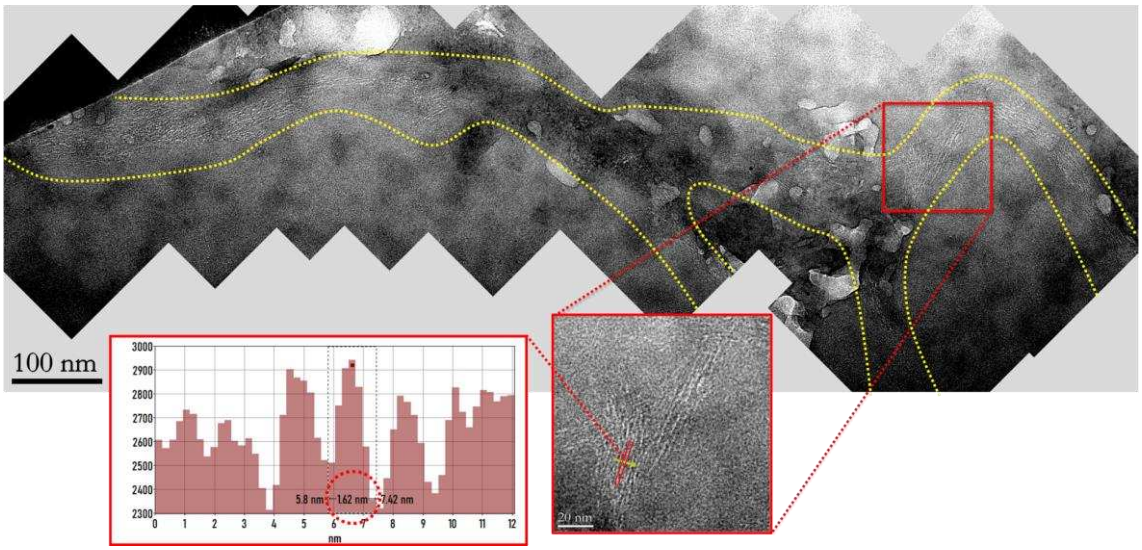

Figure 4. HRTEM image of SWCNTs' conductive network topology, embedded in the alkali activated matrix (SWCNT conc. 0.100 wt.%).

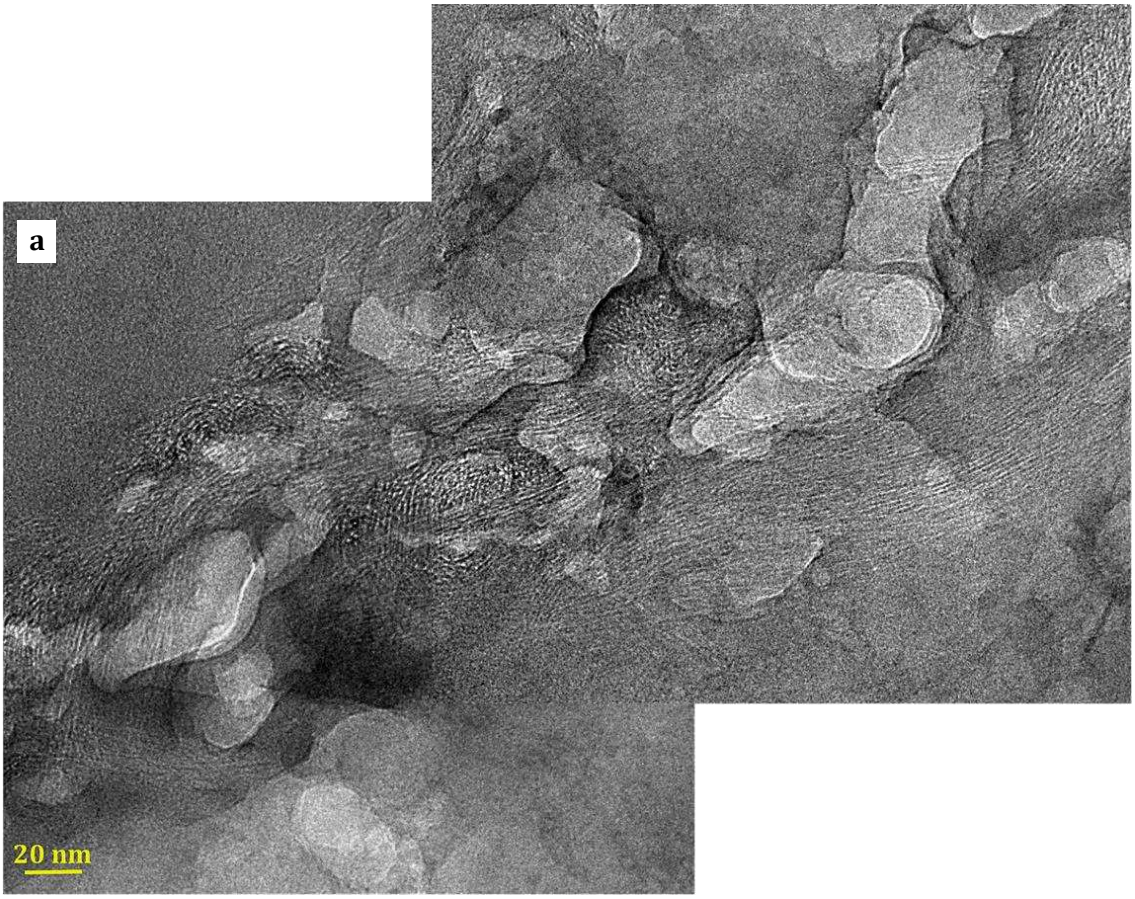

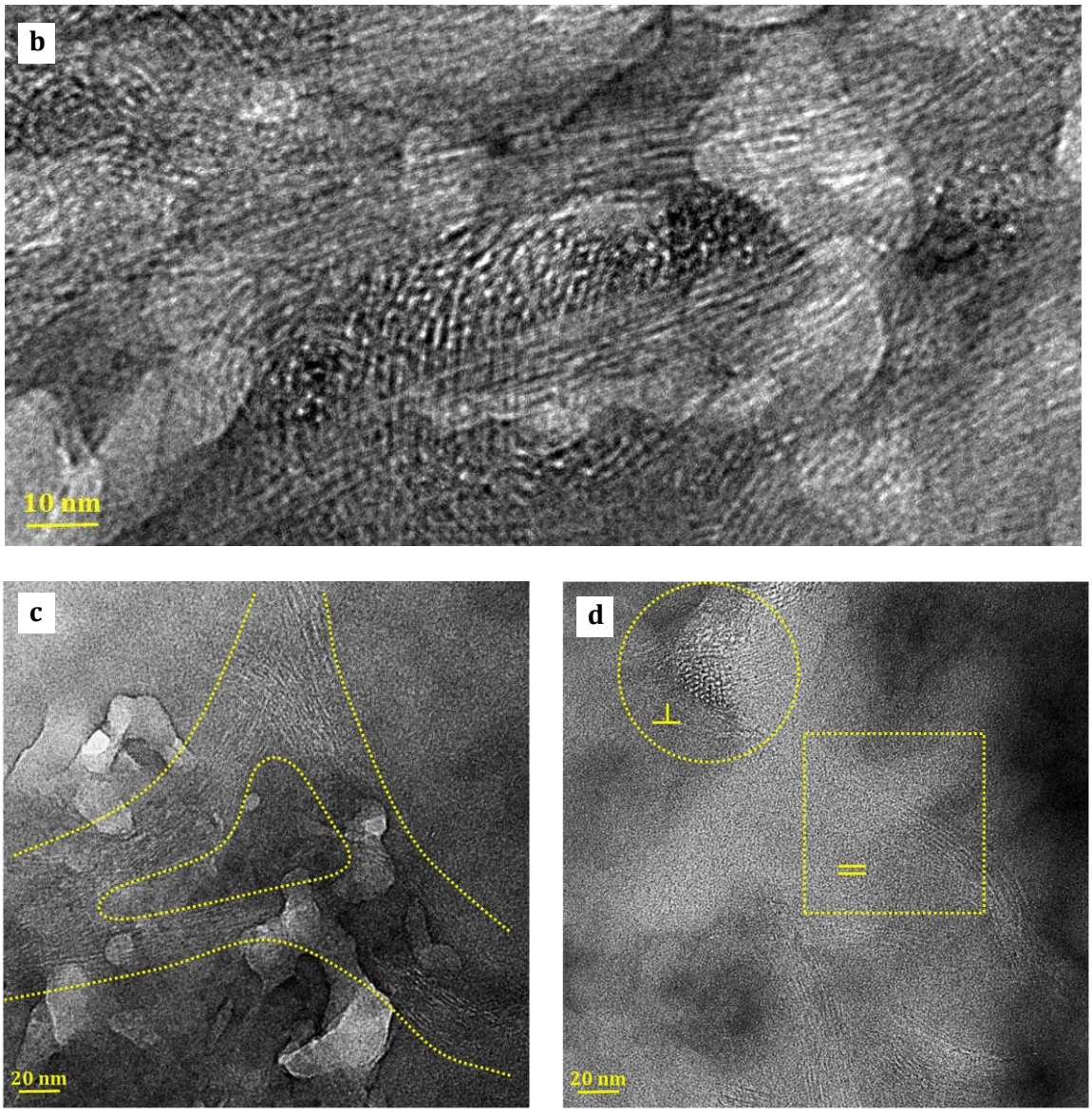

Figure 5. HRTEM images of SWCNTs' intra-network alignments throughout the alkali activated matrix (SWCNT conc. 0.100 wt.%); a- SWCNTs' alignments and conjunctions; b- higher-resolution image of the centre of a; c- SWCNTs' cross lines; d- SWCNTs' perpendicular vs. horizontal orientations.

3.3. Sensing properties

3.3.1. Exposure to ultrapure water

The signal configuration of nanocomposites upon exposure to the ultrapure water is displayed in Figure 6. The start of each cycle, water introduction, is distinguished by an abrupt increase in the relative resistance. The first cycle is from 60 s to 240 s, the second from 240 s to 480 s and the third from 480 s to 600 s, i.e., every 180 s. The 7-day sensors exhibit three times greater magnitudes of relative resistance compared to the 28 days. The maximum change of relative resistance is around 6% for 7-day nanocomposites, and 2% for 28-day nanocomposites. It is not expected SWCNTs' network to be recovered to the initial state in the short-term, i.e., the resistance of the sensor does not switch back to the original point within the investigation period. There are studies, which reported similar phenomena in sensing behaviour of the CNT-based

sensor devices, both pristine and doped [48,50,57–60]. Herein, it can be ascribed to the fact that in each cycle, the water is penetrating into the pore network and fracture system of the matrix and diffusing deeper with the onset of the next cycle, not evaporating off. Therefore, more SWCNTs will be involved in the sensing and the resistance will continue to increase. In addition to the direct interaction of water-species and the SWCNT network, the introduction of water may cause the connected tubes of adjacent CNTs to separate and relocate in the tunnelling gap or even beyond. As a consequence, the contact resistance of CNTs rose dramatically [6]. Furthermore, the water exposure may result in the leaching and mobilization of matrix alkaline cations, which were pre-suppressed by the drying process. These may additionally influence the SWCNTs' network and sensor resistance. However, this cannot yet be clarified completely in this work and will be part of a future study.

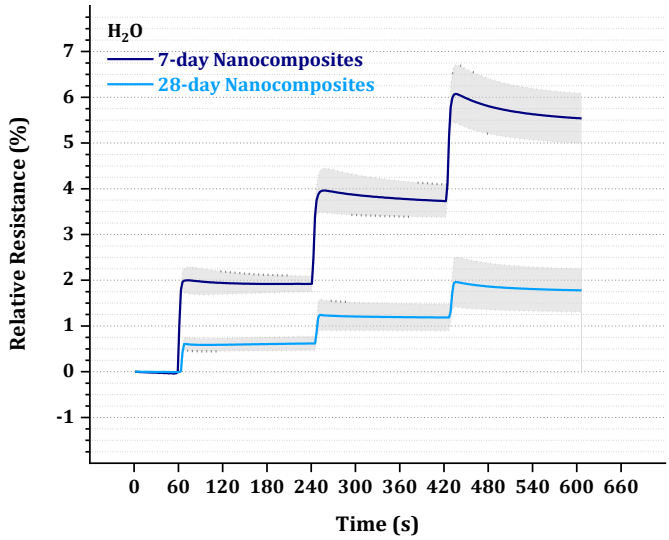

Figure 6. Sensing response of SWCNT alkali activated chemiresistors (SWCNT conc. 0.100 wt.%) after cyclic exposure to ultrapure water.

3.3.2. Exposure to sulphuric acid

The signal configurations with the variation of sulphuric acid concentration are shown in Figure 7. The sensing behaviours of the sensors by the introduction of H_2SO_4 are very different compared to the ultrapure water exposure (Figure 6). The first distinct observation is the differentiation in the shape and appearance of signals, not only in comparison to water but also in comparison to each concentration of H_2SO_4. This nonconformity puts a distinguishing boundary between high and low concentration regimes of sulphuric acid, in addition to the presence and absence of the sulphuric acid species, i.e., HSO_4^- & SO_4^{2-}, in comparison to the ultrapure water.

At the low H_2SO_4 concentration exposures, 1.00E-05 M & 1.00E-03 M, there is an almost perpendicular rise of the sensor relative resistance immediately after exposure, at the beginning of each cycle (Figure 7 a & b). This fact is valid just for the first cycle of high concentration regimes of H_2SO_4 (1.00E-01 M & 1.00E+00 M). From the second cycle, there is an initial steep reduction of the measured signals, which is accompanied by a signal rise (Figure 7 c & d). This behaviour of the

sensor is very significant in 1.00E+00 M H_2SO_4, where the amplitude of oscillations reaches approximately 5% in the last cycle (relative resistance alteration between -1% and 4%) in 7-day nanocomposites and circa 2.50% in 28-day nanocomposites (Figure 7 c & d).

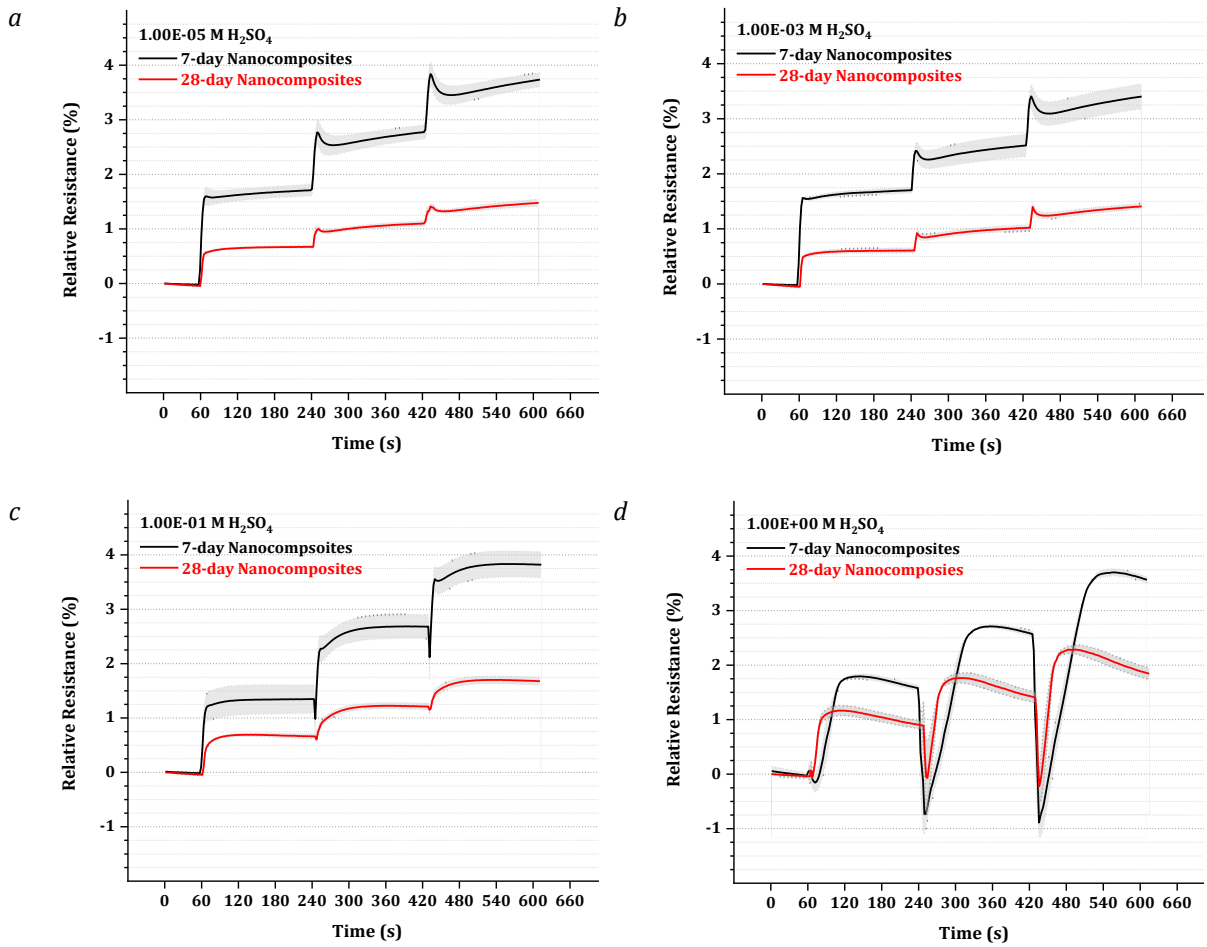

Figure 7. Sensing response of SWCNT alkali activated chemiresistors (SWCNT Conc. 0.100 wt.%) after cyclic exposure to different concentrations of sulphuric acid; a- H_2SO_4 conc. 1.00E-05 M (pH 4.70); b- H_2SO_4 conc. 1.00E-03 M (pH 2.73); c- H_2SO_4 conc. 1.00E-01 M (pH 0.97); d- H_2SO_4 conc. 1.00E+00 M (pH 0.00).

In an overall view, 7-day sensors demonstrate higher relative resistance values, as seen before in water exposure. The reasons will be elucidated in the successive section (3.4. Microstructure dependency). The maximum observed values of relative resistance in 28-day nanocomposites are ≈1.50 % for H_2SO_4 low concentration regimes (1.00E-05 M & 1.00E-03 M), >1.50% for 1.00E-01 M H_2SO_4, and >2% for 1.00E+00 M H_2SO_4. The trend for 7-day sensors reaches a magnitude of around 3.50% for all H_2SO_4 concentrations. Moreover, recovery sections in the comparison of low and high concentration regimes of H_2SO_4 represent disparate and complex trends (Figure 7).

3.3.2.1. pH influence

Sulphuric acid in aqueous solutions dissociates into hydrogen sulphate (HSO_4^-), sulphate (SO_4^{2-}), and hydronium (H_3O^+) species (Equation 1 & Equation 2), which are highly

pH/concentration dependent interactions. Based on that, investigated sulphuric acid solutions with the pre-determined concentrations and pH are composed of different concentrations of HSO_4^- and SO_4^{2-}, provided in Table 3. Therefore, in H_2SO_4 low concentration regimes (1.00E-05 M & 1.00E-03 M) the dominant species is SO_4^{2-}, while in H_2SO_4 high concentration regimes (1.00E-01 M & 1.00E+00 M), HSO_4^- is the prevalent species [61].

$$H_2SO_4 + H_2O \rightarrow H_3O^+ + HSO_4^- \qquad \textit{Equation 1}$$

$$HSO_4^- + H_2O \rightleftarrows H_3O^+ + SO_4^{2-} \qquad \textit{Equation 2}$$

Table 3. Speciation of investigated concentrations of sulphuric acid (from the results in the reference [61]).

Concentration (M)	**pH**	$\boldsymbol{HSO_4^-}$ **(%)**	$\boldsymbol{SO_4^{2-}}$ **(%)**
1.00E-05	4.70	0	100
1.00E-03	2.73	10	90
1.00E-01	0.97	75	25
1.00E+00	0.00	80	20

As mentioned above, sensors showed very distinct responses based on the concentration of introduced sulphuric acid (Figure 7). The upward trends at the begining of each cycle can be attributed to the interaction of H_3O^+ with SWCNTs. It might be possible that H_3O^+ cations can penetrate much faster into the pores and diffuse with accelerated kinetics in the internal cracks of the matrix than HSO_4^- and SO_4^{2-}. This penetration may additionally facilitate the intake of HSO_4^- and SO_4^{2-} anions in the upcoming cycles. Regarding H_2SO_4 in low concentration regimes (Figure 7 a & b), from the second cycle, SO_4^{2-} additionally penetrates and diffuses into the pores and cracks. SWCNTs transmit the same sensing signal for both H_3O^+ and SO_4^{2-}, i.e., an ascent in sensor resistance leading to an increase of relative resistance. However, in H_2SO_4 high concentration regimes (Figure 7 c & d), SWCNTs exhibit a reduction of resistance, which can be interpreted as a steep descent of relative resistance due to the HSO_4^- contact. This can be obviously seen at the beginning of the second and third cycles. This behaviour can be ascribed to the acid-base reactions of the HSO_4^- anions and the alkaline matrix of the nanocomposites, eventually yielding the SO_4^{2-} species (Equation 1 & Equation 2). Thereafter, with the increase of sulphate concentration, the upward trend of relative resistance again appears.

The pH variation resulting from the interaction of HSO_4^- and the alkali activated matrix is demonstrated in Figure 8. For these measurements, coarse-grained particles of alkaline nanocomposite were added to a sulphuric acid solution with concentration of 5.45E-02 M and pH of 1.21. Hence, in this solution, 70% of the species are HSO_4^- and the remaining 30% are SO_4^{2-} [61]. Immediately after exposure, the pH ascends dramatically to 9.54 and reaches an equilibrium at pH 10, meaning that SO_4^{2-} anions are the only species in the solution. The pH alteration has no great influence on 1.00E-05 M and 1.00E-03 M speciation because they are inherently composed

of more than 90% SO_4^{2-} species. Nonetheless, the pH of 1.00E-01 M and 1.00E+00 M H_2SO_4 undergoes acid-base neutralization, i.e., shifting the pH from acidic to basic values (Figure 8).

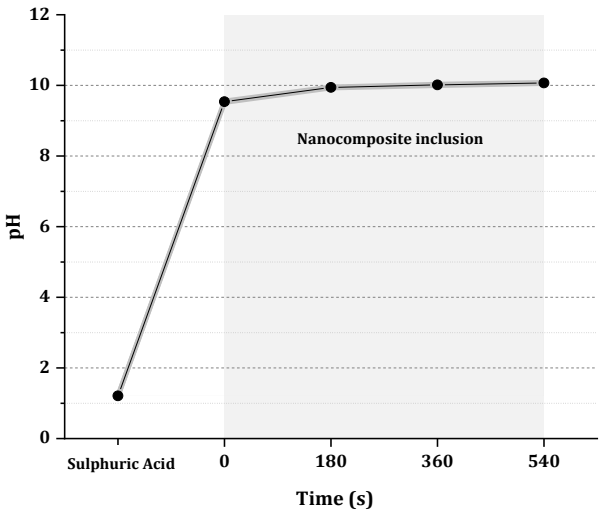

Figure 8. pH measurements of SWCNT alkali activated nanocomposites (SWCNT conc. 0.100 wt.%) and sulphuric acid 5.45E-02 M (exposure simulation experiment).

This dual response of SWCNTs in the exposure to an analyte, an initial descent followed by a secondary ascent, has never been reported in the literature. As explained above, the reason is the synergistic interactions of the alkali activated matrix and SWCNTs. According to the published literature, SWCNTs experience an increase in conductivity in exposure to an oxidising dopant, e.g., NO_2 & Cl_2 and a decrease, in the presence of a reducing dopant, e.g., NH_3 & H_2 [6,8,62–64]. H_2SO_4 is a strong electron acceptor and oxidative dopant (p-dopant) of SWCNTs and it can enrich the hole concentration of SWCNTs by the protonation of the tubes (due to the presence of HSO_4^-) [57,65]. Furthermore, HSO_4^- consumption as a consequence of the acid-base neutralization effect of the alkaline matrix, and production of SO_4^{2-}species generates a scenario, which simulates the addition of an electron donor and reducing dopant (n-dopant) to the SWCNTs. Hence, herein, two consecutive mechanisms of charge transport between sulphuric acid species and SWCNTs are implemented.

3.3.2.2. Surface composition change

The FTIR-spectra and correlation peak assignments of the sensors before (pristine) and after exposure to sulphuric acid are shown in Figure 9 and Table 4. In an overall view, both 7 and 28 days pristine nanocomposites share the most features of FTIR-spectra; hence, there is not any significant age-dependency of the nanocomposites surface composition. Nevertheless, the significant differences between pristine (black spectra in Figure 9) and sulphuric acid exposed (red spectra in Figure 9) sensors are present in i) the $Si-O-R$ stretching region, ii) the $R-OH$ stretching and bending regions, and iii) the $O-C-O$ stretching region. Moreover, the bands

ascribable to the SWCNTs and SDBS are mostly indiscernible because of the high intensity of the alkali activated core framework bands ($Si - O - R$ & $R - OH$).

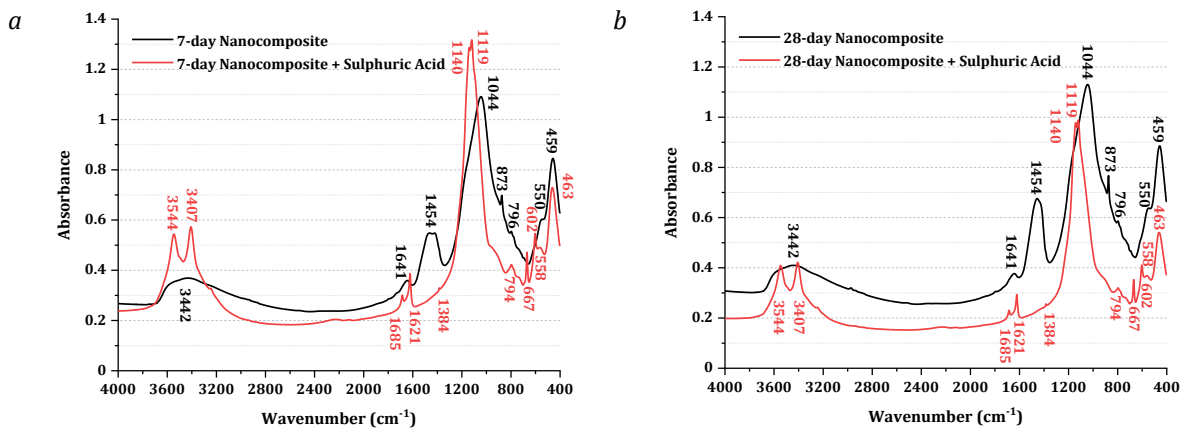

Figure 9. FTIR spectra of SWCNT alkali activated nanocomposites (SWCNT conc. 0.100 wt.%) before (black line) and after sulphuric acid exposure (red line); a- 7-day nanocomposites; b- 28-day nanocomposites.

Considering the acid exposed red spectra in Figure 9 a & b, SO_4^{2-} (probably adsorbed on the surface pores) are detectable in 700 cm^{-1}-580 cm^{-1} with two peaks, which are not present in the pristine specimens (black spectra in Figure 9 a & b). The peaks at 667 cm^{-1} and 602 cm^{-1} correspond to the bending vibrations of $S = O$ and $S - O$ bonds of SO_4^{2-} species. The stretching vibrations of these species appear in an overlapped state (combined with $Si - O - R$ bands of core material) at 1140 cm^{-1} and 1119 cm^{-1} of the acid exposed red spectra. Furthermore, the characteristic bond vibrations of SO_3^- groups of SDBS should appear at ≈550+ cm^{-1} (bending), ≈1000+ cm^{-1} (symmetric stretching), and ≈1100+ cm^{-1} (asymmetric stretching) are not detectable due to the low concentration of SDBS in the matrix. Likewise, the aromatic carbon ring vibrations of SDBS, for instance, the stretching vibrations at ≈1600 cm^{-1} ($C \overset{\cdots}{=} C$ ring quadrant) and ≈1400/1500 cm^{-1} ($C \overset{\cdots}{=} C$ ring semicircle), are not detectable [66–69].

The most intense absorbance band of the framework (1340 cm^{-1} - 650 cm^{-1}) is positioned at 1044 cm^{-1}, which is attributed to the asymmetric stretching of the tetrahedral $Si - O - R$ bonds (R represents Si or Al) of the alkali activated ($N - (C) - A - S - H$) and geopolymeric ($N - A - S - H$) phases of the material core. The related symmetric stretching vibration of the material core is located at 796 cm^{-1} in the form of a weak sharp shoulder structure. The bending vibrations of the core $Si - O - R$ tetrahedra, a strong absorbance band, is observed at 459 cm^{-1} due to the $Si - O$ vibrations including $Al - O$ shoulder (overlapped) at 550 cm^{-1} [28,29,70–72].

Sulphuric acid exposed material exhibits a shift of the core band toward higher frequencies, between 1570 cm^{-1} - 840 cm^{-1} centering at 1140 cm^{-1} & 1119 cm^{-1}, which is due to the SO_4^{2-} coverage [29]. The stretching shoulder of $Si - O - Si$ or $Si - O - Al$ bonds is detectable with a slight shift to 794 cm^{-1}. A broad weak band at 558 cm^{-1} can be ascribed to the $Al - O$ shoulder [70]. The bending vibration mode of the core at 463 cm^{-1} is not affected strongly by the

acid exposure. The core band shift, accompanied by the appearance of a new band at 670 cm^{-1}, were additionally assigned to the presence of gypsum ($CaSO_4.2H_2O$) in the references [28,70] for long-term immersions. Herein, the introduced quantity of sulphuric acid was 30 µL per cycle (a total of 90 µL of concentrated acid). Hence, during the short-term exposure to the extreme acidic environment, the core material could not be highly destroyed. Nonetheless, the aforementioned band shifts represent a potential deterioration of the material bonds, perhaps a slight core dealumination or decalcification [28,29].

Table 4. FTIR correlation band data of nanocomposites (SWCNT conc. 0.100 wt.%); 7 and 28 days nanocomposites represent the same values; R corresponds to the tetrahedral Si or Al.

Nanocomposite			**Nanocomposite + Sulphuric Acid**		
Range (*cm^{-1}*)	**Center (*cm^{-1}*)**	**Vibration**	**Range (*cm^{-1}*)**	**Center (*cm^{-1}*)**	**Vibration**
2500-3700	3442	$R-OH\ (str.)$	2700-3700	3544 & 3407	$R-OH\ (str.)$ & $O-H\ (str.)$
1600-1700	1641	$R-OH\ (bend.)$	1570-1720	1621 & 1685	$R-OH\ (bend.)$ & $O-H\ (bend.)$
1600-1350	1454	$O-C-O\ (asym.str.)$	1391-1376	1384	$O-C-O\ (sh.)$
1340-650	1044	$Si-O-R\ (asym.str.)$ ($SO_3^-\ str.$)	1570-840	1140 & 1119	$Si-O-R\ (asym.str.)$ $S=O$ & $S-O$ (SO_4^{2-} /$SO_3^-str.$)
885-864	873	$O-C-O\ (bend.)$	disappeared		
814-764	796	$Si-O-R\ (sh.)$ ($sym.str.$)	840-700	794	$Si-O-R\ (sh.)$ ($sym.str.$)
not detected			700-651	667	$S=O\ (SO_4^{2-}\ bend.)$
			651-580	602	$S-O\ (SO_4^{2-}\ bend.)$
579-527	550	$Al-O\ (sh.)$ ($SO_3^-\ bend.$)	580-527	558	$Al-O\ (sh.)$ ($SO_3^-\ bend.$)
650-400	459	$Si-O\ (bend.)$	527-400	463	$Si-O\ (bend.)$

The sharp band at 1454 cm^{-1} and the 873 cm^{-1} shoulder of the pristine samples (black spectra in Figure 9 a & b) are attributable to the vibrations of carbonate species (CO_3^{2-}). CO_3^{2-} species undergo acid-base neutralization reactions in the presence of sulphuric acid. Consequently, the 1454 cm^{-1} band was converted to a weak shoulder at 1384 cm^{-1}, while the 873 cm^{-1} shoulder disappeared in the acidified specimens. The $O-C-O$ band at 1454 cm^{-1} is relatively strong because of the ambient curing of nanocomposites and the potential availability of the coordinating Ca^{2+} in the alkali activated framework, which can result in the fast formation of polymorphs of $CaCO_3$[73,74].

Regarding the strong vibrations of the $Si-O-R$ at 1340 cm^{-1} - 650 cm^{-1}, the polycondensated core displays two other distinct $R-OH$ absorbance bands in the pristine nanocomposites (black spectra in Figure 9 a & b). The stretching of $R-OH$ appears in a very

broad band (from 2500 cm^{-1} to 3700 cm^{-1}) centred at 3442 cm^{-1}. The much narrower and weaker bending mode is located in between 1600 cm^{-1} and 1700 cm^{-1} with the centre at 1641 cm^{-1}. Upon exposure to sulphuric acid, both of these bands split into two sharp bands with stretching poles at 3544 cm^{-1} and 3407 cm^{-1} and bending peaks at 1621 cm^{-1} and 1685 cm^{-1} [28,29,70,71,75,76]. The appearance of these double peaks can be ascribed to the formation of $CaSO_4.2H_2O$, as reported in reference [28] for long-term immersions and in reference [77].

3.3.3. Sensor sensitivity

The correlation between the cumulative relative resistance and sulphuric acid concentration, and correspondingly the sensitivity of chemiresistors are represented in Table 5, Table 6, & Figure 10. The 7-day chemiresistors are superior in comparison to the 28 days with higher fractional changes and sensitivities. Furthermore, the fractional changes and sensitivities have a direct relationship with the sulphuric acid concentrations. The highest values are obtained for concentrated sulphuric acid regimes, i.e., 1.00E-01 M and 1.00E+00 M, and on the contrary, sensors do not exhibit significant sensitivity differences in low concentration regimes of sulphuric acid, i.e., 1.00E-05 M and 1.00E-03 M.

Table 5. Cumulative relative resistance changes in SWCNT alkali activated chemiresistors (SWCNT conc. 0.100 wt.%).

H_2SO_4 Concentration (M)	Sensitivity (%)	
	7-day nanocomposites	28-day nanocomposites
H_2O	6.10 ± 0.63	1.96 ± 0.45
1.00E-05	3.85 ± 0.21	1.53 ± 0.06
1.00E-03	3.44 ± 0.22	1.43 ± 0.07
1.00E-01	5.71 ± 0.42	1.99 ± 0.27
1.00E+00	15.99 ± 1.53	7.57 ± 0.68

Table 6. Sensitivity of SWCNT alkali activated chemiresistors (SWCNT conc. 0.100 wt.%).

H_2SO_4 Concentration (M)	Sensitivity (absolute value)					
	7-day nanocomposites			28-day nanocomposites		
1.00E-05	0.0042			0.0009		
1.00E-03		0.0229			0.0056	
1.00E-01			1.1426			0.6194
1.00E+00						

The chemiresistors have a relative resistance/resistance surge in both 7-day and 28-day nanocomposites due to the exposure to the 1.00E+00 M sulphuric acid, of ca. 16% and 8%, respectively (Figure 10). The presence of potential leaching matrix material anions and cations might restrain the newly introduced ions penetration and diffusion into the pore-crack system of

the alkali activated microstructure. Consequently, the SWCNTs might not encounter sufficient quantities of analyte to generate and transmit a significant signal, but the observations indicate contradictory results, possibly indicating a non-significant ion leaching. In this respect, it appears that the alkali activated sensors have no limitation in the high detection threshold.

The relative resistance function of alkali activated chemiresistors shows a curvilinear outline with a stationary point at 1.00E-03 M, which can be the sensor's lower detection threshold (Table 5 & Figure 10). From the curve stationary point toward higher concentrations, the relative resistance change and sensitivity of the sensors with an increase in sulphuric acid concentration is exponentially rising. The 7- day sensitivity is ≈0.02 for concentration range of 1.00E-03 M - 1.00E-01 M, and ≈1.1 for the range of 1.00E-01 M - 1.00E+00 M (Table 6). This means that the sensor is able to discriminate more accurately between medium to high sulphuric acid concentrations than low concentrations. Moreover, this pH/concentration range is of interest to the researchers working on concrete durability due to the sulphuric acid exposure. The pH of 0.800 [29], 1 [78–80], and 2 [78,79,81], and the concentration of 0.001 [82] have been studied in the relevant literature.

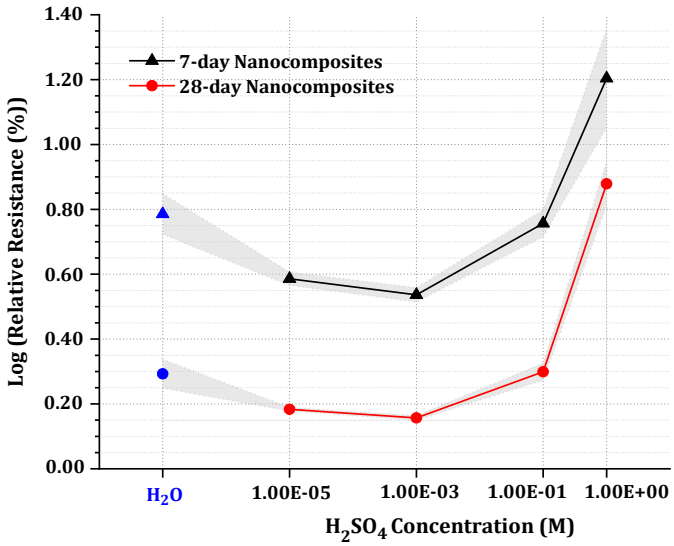

Figure 10. Correlation of cumulative relative resistance of SWCNT alkali activated chemiresistors and introduced H_2SO_4 concentrations (SWCNT conc. 0.100 wt.%).

Notwithstanding that discrimination capability, because of the convex shape of the function, the relative resistance change of high-concentrated sulphuric acids may correspond to very low-concentrated ones, i.e., attributable to water or moisture. For instance, the change percentage of 1.00E-01 M sulphuric acid and ultrapure water is approximately the same. However, their response signal shapes still are obviously recognizable (Figure 7 c & Figure 6). Therefore, assessing a combination of original resistance signals and normalized values can be an asset for a more precise analyte discrimination.

3.4. Microstructure dependency

3.4.1. SWCNTs and matrix interactions

The sensing properties of the SWCNT alkali activated chemiresistors are significantly influenced by the physical interactions between SWCNTs and the matrix, considering the microstructure characteristics of the alkali activated materials. SWCNTs' fractal and three-dimensional propagation in the matrix, hole lining and coverage, cavities and fractures bridging, agglomeration geometry, and embedment degree can be counted as dominant factors regarding sensing behaviour of the chemiresistors. The SWCNTs' propagation, the fractal spread and escalation of SWCNTs were depicted previously in Figure 3.

The existence of micron-scale holes and cavities in the matrix can interrupt the SWCNTs' networking efficiency if not covered by or connected to the surrounding network members. The utilized SWCNTs herein have a length of ≈5 μm, however, this length can be extended to ≥10+ μm considering the agglomeration geometry and configuration of SWCNTs (Figure 11 a). According to Figure 11 a, a giant hole is covered by the SWCNTs' network members at a length of 10 μm and 15 μm. The hole's interior surface is additionally lined with fabric-like SWCNTs, marked by a yellow arrow in the image, evidencing the SWCNTs' conductive network consistency. In addition to the mentioned mechanism, long span cavities are bridged by SWCNTs as illustrated in Figure 11 b. The conductive network consistency is retained here by ≈5 μm long aligned SWCNTs which densely bridge a 20-micron-span cavity.

a

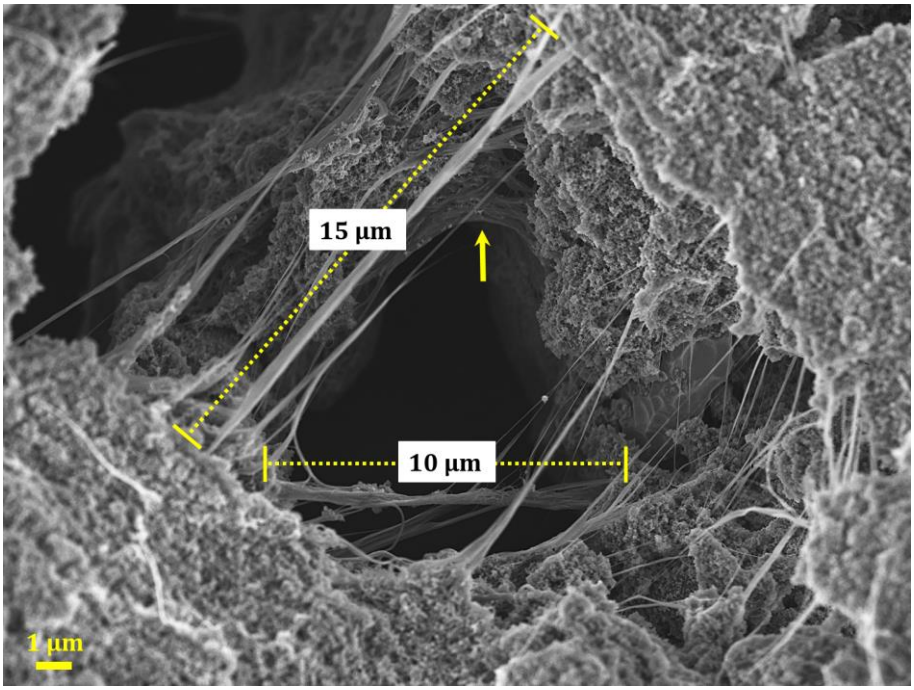

b

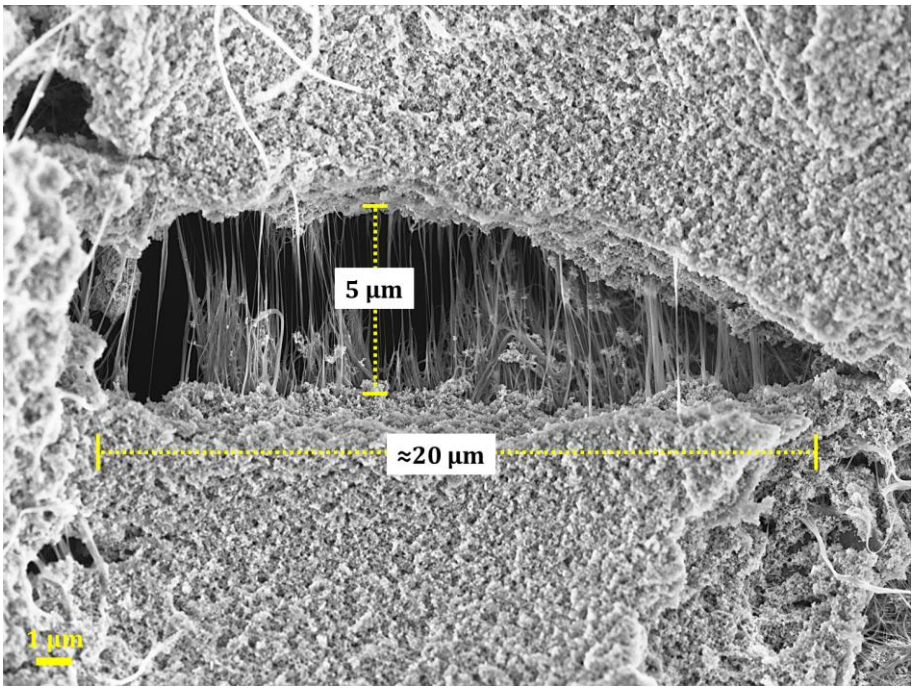

Figure 11. Conductive network integrity maintenance of SWCNTs (SWCNT conc. 0.100 wt.%); a- hole surface lining and coverage by SWCNTs; b- dense bridging of a cavity by aligned SWCNTs.

Embedment of SWCNTs into the matrix material determines the accessibility degree of SWCNTs by analytes and consequently the intensity of transmitted signals. Since the inert SWCNTs have reactive SDBS in the vicinity, it is highly probable that they are extemporaneously involved in the core formation and become a constituent part of the framework. Depending on the evolution of the matrix, SWCNTs will be incorporated more intensively into the microstructure; therefore, SWCNTs in 28-day nanocomposites look more entangled (Figure 12 c) or deeply buried (Figure 12 d) in comparison to the 7-day counterparts (Figure 12 a & b). Even in several parts of 28-day nanocomposites, SWCNTs contributed to the skeleton of the core framework, where they are not highly agglomerated (Figure 12 d vs c). Such ageing behaviours are highly advantageous for the electrical (Table 1) and mechanical improvements [45] but they have a negative impact on the sensing capacity of SWCNTs (Figure 7 & Figure 10). As explained before, 28-days sensors had better conductivity but worse sensing capability. Because the huge surface area of SWCNTs is partially or completely covered by the core alkali activated material and is not accessible by the analytes. As shown in Figure 12 a & b, several spontaneously aligned SWCNTs are found in the 7-day nanocomposites that expose enormous free surfaces to the analyte.

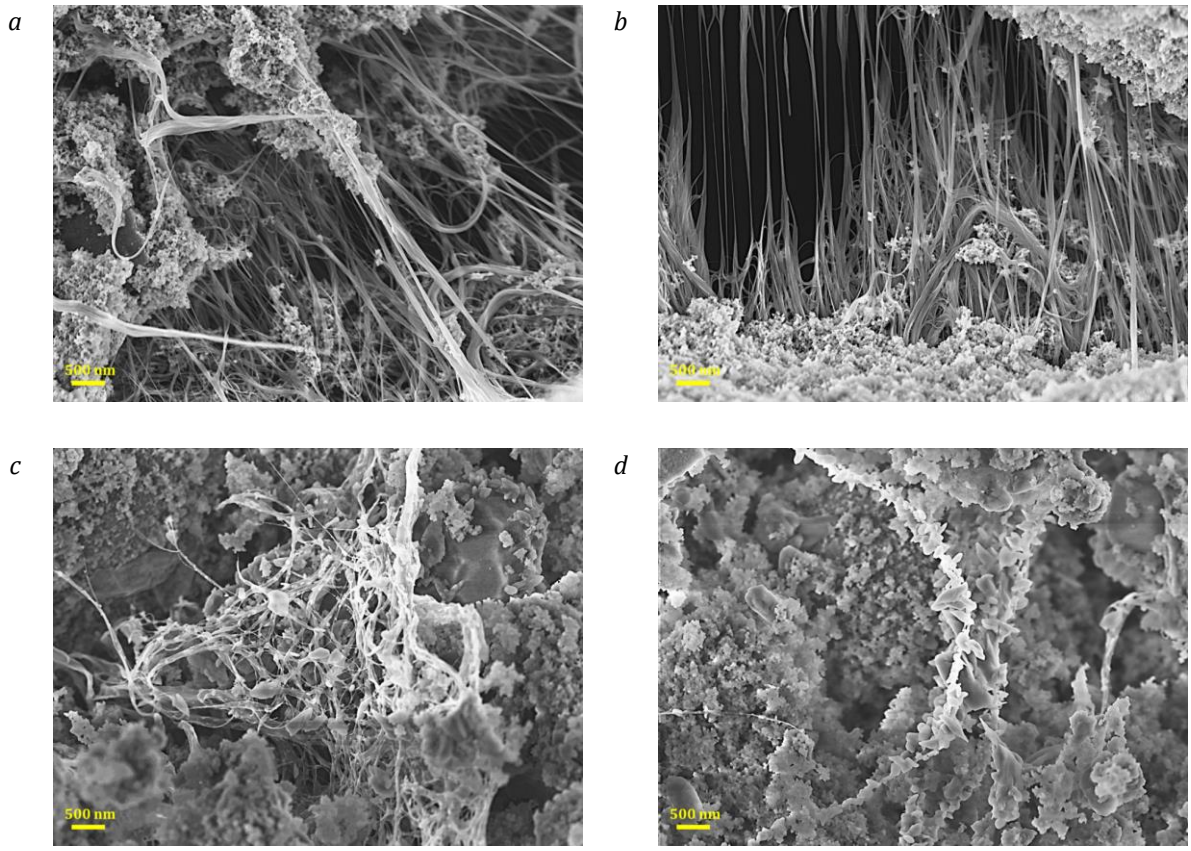

Figure 12. SWCNTs interactions with the alkali activated matrix (SWCNT conc. 0.100 wt.%); a & b- aligned SWCNTs in 7-day nanocomposites; c- entangled and partially covered SWCNTs in 28-day nanocomposites; d- completely covered SWCNTs in 28-day nanocomposites.

3.4.2. Matrix porosity

The porosity of 7-day and 28-day nanocomposites exhibit approximately very similar distributions (Figure 13), therefore, it cannot be used to explain sensing behaviours. The applied ambient curing can be the main impetus of this occurrence, similar to what observed in FTIR spectrometry of the nanocomposites (Figure 9). The total porosity of sensors is almost 45%, and their cumulative pore volume reaches around 320 $mm^3.g^{-1}$. The most frequent pore dimensions of nanocomposites are located in a broad pore span of 40 nm to 2 μm with two distinct peaks for 7 days at 165 nm and 600 nm, and for 28 days at 180 nm and 700 nm. This substantiates a compact nanostructure but a porous microstructure of the material because of the abundance of capillary and air-entrained pores as demonstrated by SEM images in the previous sections.

The porosity level is an essential prerequisite of the herein proposed class of sensors and it should even be increased to a greater degree. A higher number of pathways and channels throughout the sensor will allow the analyte to reach the embedded SWCNTs with much faster kinetics. The alkali activated nanocomposites in previously published work [45], demonstrated a cumulative pore volume of approximately a third less (≈100 $mm^3.g^{-1}$) with the most frequent pore size located in <10 nm region i.e., a porous nanostructure but a compact microstructure. This huge favourable increase of this-research porosity is attributable to the destructive impacts of SBDS on the material microstructure, both chemically (constitution of less binding material) and physically

(air bubbles entrapment) in comparison to the previously utilized surfactant, naphthalene sulfonate. The fabrication methodology has furthermore significant influence herein, i.e., using one-part technology and ambient curing methodology.

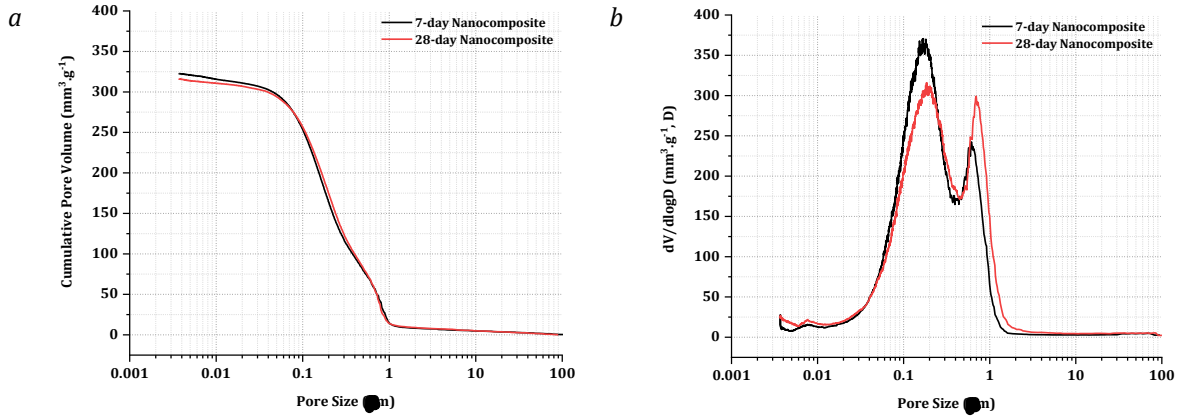

Figure 13. Porosity analysis (MIP) of SWCNT alkali activated nanocomposites (SWCNT conc. 0.100 wt.%); a- cumulative distribution; b- differential distribution.

3.4.3. Matrix roughness

Notwithstanding the pore distributions (Figure 13), the topography and profile characteristics of 7-day and 28-day nanocomposites show a considerable contrast (Figure 14 a vs b). The 7-day nanocomposites have a much higher roughness compared to the 28-day nanocomposites, which exhibit a relatively smoother surface. According to the profile mapping of the 7-day nanocomposites, there are many facial micro-cavities penetrating as deep as 80 μm into the body of specimens (Figure 14 a). Those cavities are composed of many air holes and fractures on the surface texture of the nanocomposites, which could be detected effortlessly by SEM (Figure 15). The cavities could provide required pathways for inflow and diffusion of sulphuric acid species and water into the alkali activated sensor bulk mass and increase the probability of interactions with the SWCNTs exterior tubes. This phenomenon is observed to a very lesser extent in the 28-day nanocomposites. Mainly, the topography of 28-day nanocomposites consists of many height fluctuations and deviations, i.e., relief, within a range of ±20 μm according to Figure 14 b, resulting in a great operational difficulty in the topography observations by the SEM.

As explained, the topography of 7-day nanocomposites composed of fractures and air holes. In particular, most of the facial fractures are covered or bridged by the SWCNTs, which put forward additional assistance to the sensing features of the 7-day nanocomposites (Figure 15 a & b). On the contrary, observed air holes were principally CNT-free and merely participated in the penetration of sulphuric acid and water into the bulk mass of the sensor (Figure 15 c & d). Altogether, the highly fractured and rough profile of 7-day sensors results in accelerated analyte diffusion into the alkali activated microstructure. Furthermore, in the bulk mass of the 7-day nanocomposites, less covered and buried SWCNTs are more accessible (Figure 12) and able to

release the signals with higher intensity (Figure 6, Figure 7 & Figure 10) in comparison to the 28-day nanocomposites.

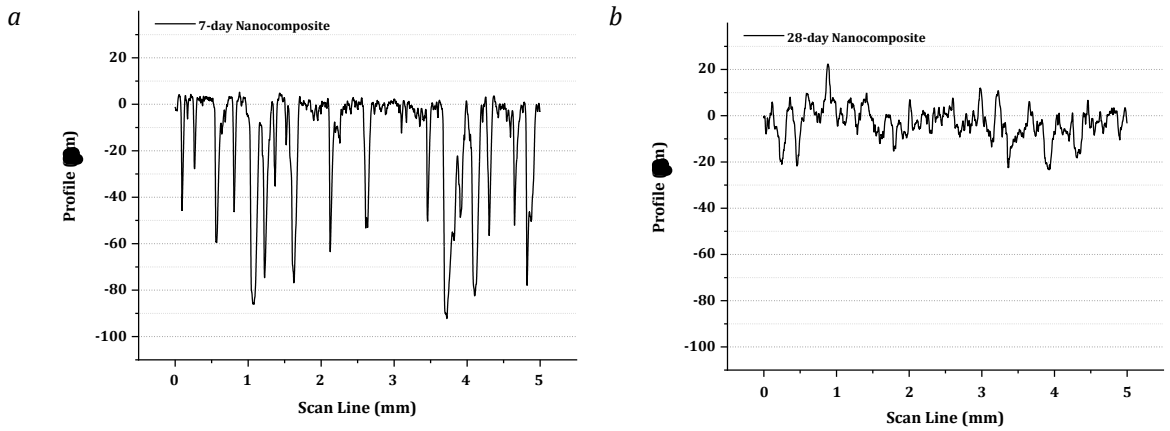

Figure 14. Profile mapping and roughness of SWCNT alkali activated nanocomposites (SWCNT conc. 0.100 wt.%); a- 7-day nanocomposites; b- 28-day nanocomposites.

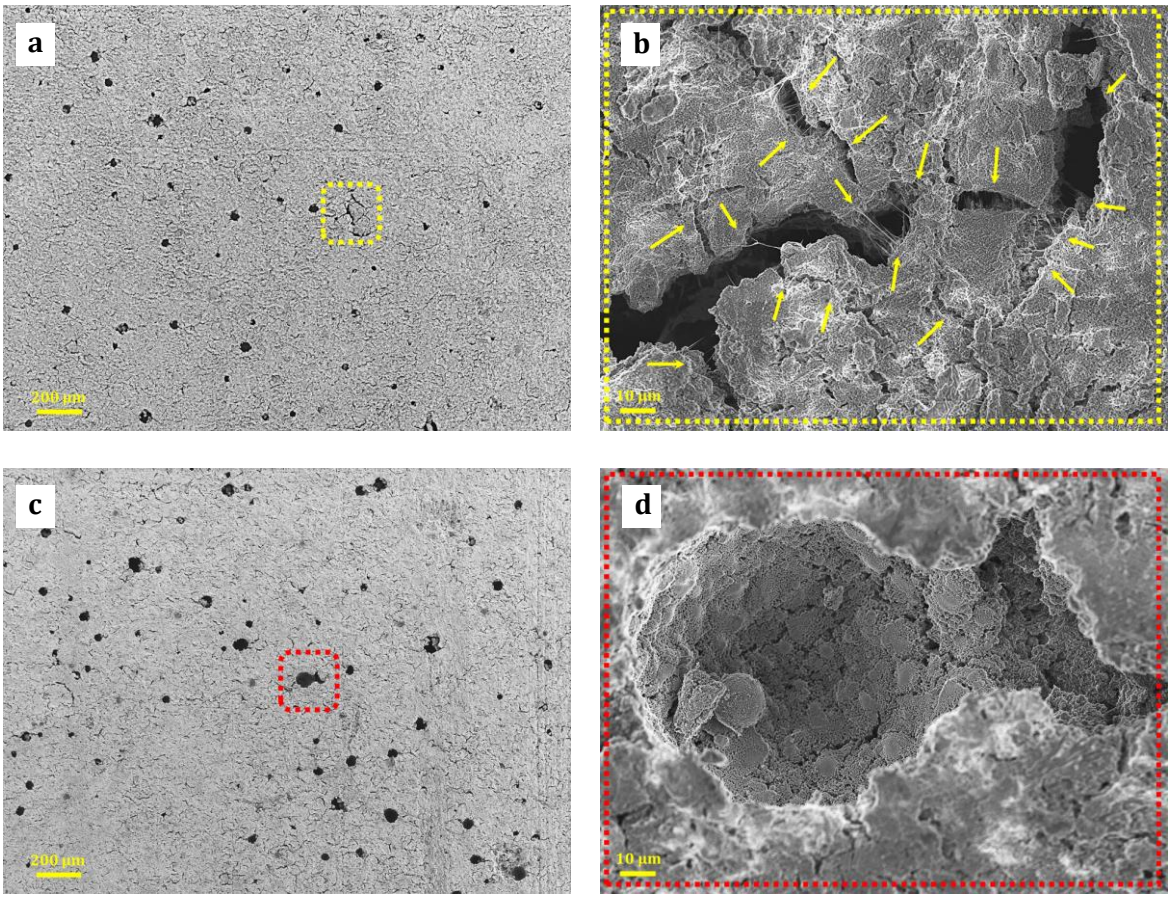

Figure 15. Topography of two different areas of the SWCNT alkali activated 7-day nanocomposites (a & c) (SWCNT conc. 0.100 wt.%); c- magnified image of the surface cavities and fractures: filled with SWCNTs; d- magnified image of the air holes: not covered by SWCNTs.

4. Conclusion and outlook

An innovative and unconventional H_2SO_4 sensing concept for the SWCNT alkali activated chemiresistors has been created in this research. An electronic conductive network was

established by incorporating SWCNTs into the sodium-based fly-ash-GGBS alkali activated matrix. The developed chemiresistors could generate discriminative signals upon sulphuric acid and water exposures. Based on the conducted measurements and characterizations, it can be concluded that:

- The chemiresistors' conductivity with incorporation of 0.100 wt.% SWCNT are 4.80 $S.m^{-1}$ for 7-day nanocomposites and 6.02 $S.m^{-1}$ for 28-day nanocomposites.
- The chemiresistors sense the existence and differentiate the concentration of H_2SO_4 species by transmitting distinguishable signals. The H_2SO_4 low detection threshold is 1.00E-03 M in concentration and 2.73 in pH.
- The 7-day sensors convey more intensified signals than 28 days, because SWCNTs are more accessible through pathways and less buried under the core material.
- The alkali activated material and sulphuric acid have mutual interactions. The pH of H_2SO_4 is neutralized after exposure to the matrix alkaline environment, resulting in HSO_4^- consumption and SO_4^{2-} production. In parallel, the core material of the alkali activated matrix appears to be susceptible to a slight deterioration due to H_2SO_4 exposure.

The described mechanisms and accomplished results can be considered as a conceptual study for the development of a quantified and discriminative SWCNT alkali activated sensor for aggressive ion detection. Considering the concrete infrastructures' operational lifespan, sensor long-term behaviour and recovery, and matrix durability regarding corrosive ion penetration to the material microstructure would be attractive issues.

Acknowledgement

The authors would like to cordially acknowledge and appreciate all colleagues participating in this research. Ms. Almut Pöhl for TEM; Dr. Bernd Rellinghaus and Mr. Alexander Than for SEM; Mr. Marco Naumann for FTIR; Ms. Annett Willomitzer for MIP; Dr. Katherina Haase and Mr. Jonathan Perez Andrade for profile mapping; and Dr. Mahdi Samadi Khoshkhoo for proof reading of the manuscript.

Funding and facilities

The research was co-financed by tax funds based on the budget adopted by the Saxon State Parliament. The research facilities have been provided by Chair of Materials Science and Nanotechnology, Dresden Centre for Nanoanalysis, and Leibniz Institute for Solid State and Materials Research.

References

[1] E. Llobet, Gas sensors using carbon nanomaterials: A review, Sensors and

Actuators B: Chemical 179 (2013) 32–45.

[2] N.C. Karmakar, T. Athauda, J.K. Saha, Smart Materials for Sensing, in: Encyclopedia of Smart Materials, Elsevier, 2022, pp. 267–287.

[3] A.K. Sharma, A.K. Debnath, D.K. Aswal, A. Mahajan, Room temperature ppb level detection of chlorine using peripherally alkoxy substituted phthalocyanine/SWCNTs based chemiresistive sensors, Sensors and Actuators B: Chemical 350 (2022) 130870.

[4] N. Shehata, E.T. Sayed, M.A. Abdelkareem, G.A. Ali, A.-G. Olabi, Smart Electronic Materials, in: Encyclopedia of Smart Materials, Elsevier, 2022, pp. 300–309.

[5] Y. Li, M. Hodak, W. Lu, J. Bernholc, Mechanisms of NH3 and NO2 detection in carbon-nanotube-based sensors: An ab initio investigation, Carbon 101 (2016) 177–183.

[6] V. Schroeder, S. Savagatrup, M. He, S. Lin, T.M. Swager, Carbon Nanotube Chemical Sensors, Chemical reviews 119 (2019) 599–663.

[7] Z. Wang, W. Ma, J. Wei, K. Lan, S. Yan, R. Chen, G. Qin, High-performance olfactory receptor-derived peptide sensor for trimethylamine detection based on Steglich esterification reaction and native chemical ligation connection, Biosensors & bioelectronics 195 (2022) 113673.

[8] O.V. Sedelnikova, V.I. Sysoev, O.A. Gurova, Y.P. Ivanov, V.O. Koroteev, R. Arenal, A.A. Makarova, L.G. Bulusheva, A.V. Okotrub, Role of interface interactions in the sensitivity of sulfur-modified single-walled carbon nanotubes for nitrogen dioxide gas sensing, Carbon 186 (2022) 539–549.

[9] L. Sacco, S. Forel, I. Florea, C.-S. Cojocaru, Ultra-sensitive NO2 gas sensors based on single-wall carbon nanotube field effect transistors: Monitoring from ppm to ppb level, Carbon 157 (2020) 631–639.

[10] B. Yoon, S.-J. Choi, Selective acetate recognition and sensing using SWCNTs functionalized with croconamides, Sensors and Actuators B: Chemical 346 (2021) 130461.

[11] F. Shoghi, S. Mal, M. Tie, A. Badia, R. Martel, pH responsive platinum-coated single-walled carbon nanotube optical sensor with internal reference, Carbon 184 (2021) 659–668.

[12] M. Inaba, T. Oda, M. Kono, N. Phansiri, T. Morita, S. Nakahara, M. Nakano, J. Suehiro, Effect of mixing ratio on NO2 gas sensor response with SnO2-decorated carbon nanotube channels fabricated by one-step dielectrophoretic assembly, Sensors and Actuators B: Chemical 344 (2021) 130257.

[13] F. Yin, W. Yue, Y. Li, S. Gao, C. Zhang, H. Kan, H. Niu, W. Wang, Y. Guo, Carbon-based nanomaterials for the detection of volatile organic compounds: A review, Carbon 180 (2021) 274–297.

[14] C. Grengg, N. Ukrainczyk, G. Koraimann, B. Mueller, M. Dietzel, F. Mittermayr, Long-term in situ performance of geopolymer, calcium aluminate and Portland cement-based materials exposed to microbially induced acid corrosion, Cement and Concrete Research 131 (2020) 106034.

[15] M. Kobayashi, K. Takahashi, Y. Kawabata, Physicochemical properties of the Portland cement-based mortar exposed to deep seafloor conditions at a depth of 1680 m, Cement and Concrete Research 142 (2021) 106335.

[16] R.O. Abdel Rahman, M.I. Ojovan, Sustainability of cementitious structures, systems, and components (SSC's): Long-term environmental stressors, in: R.O.A. Rahman, M.I. Ojovan (Eds.), Sustainability of life cycle management for nuclear cementation-based technologies, Woodhead Publishing, Oxford, 2021, pp. 181–232.

[17] M.I. Ojovan, W.E. Lee, S.N. Kalmykov, Immobilisation of Radioactive Waste in Cement, in: M.I. Ojovan, W.E. Lee, S.N. Kalmykov (Eds.), An introduction to nuclear waste immobilisation, Elsevier, Amsterdam, 2019, pp. 271–303.

[18] A. Paul, M. Rashidi, J.-Y. Kim, L.J. Jacobs, K.E. Kurtis, The impact of sulfate- and sulfide-bearing sand on delayed ettringite formation, Cement and Concrete Composites 125 (2022) 104323.

[19] Y. Gu, P. Dangla, R.-P. Martin, O. Omikrine Metalssi, T. Fen-Chong, Modeling the sulfate attack induced expansion of cementitious materials based on interface-controlled crystal growth mechanisms, Cement and Concrete Research 152 (2022) 106676.

[20] M. Hlobil, K. Sotiriadis, A. Hlobilová, Scaling of strength in hardened cement pastes - Unveiling the role of microstructural defects and the susceptibility of C-S-H gel to physical/chemical degradation by multiscale modeling, Cement and Concrete Research 154 (2022) 106714.

[21] M.W. Kiliswa, K.L. Scrivener, M.G. Alexander, The corrosion rate and microstructure of Portland cement and calcium aluminate cement-based concrete mixtures in outfall sewers: A comparative study, Cement and Concrete Research 124 (2019) 105818.

[22] T. Yang, X. Gao, J. Zhang, X. Zhuang, H. Wang, Z. Zhang, Sulphate resistance of one-part geopolymer synthesized by calcium carbide residue-sodium carbonate-activation of slag, Composites Part B: Engineering 242 (2022) 110024.

[23] G. Zhang, C. Wu, D. Hou, J. Yang, D. Sun, X. Zhang, Effect of environmental pH values on phase composition and microstructure of Portland cement paste under sulfate attack, Composites Part B: Engineering 216 (2021) 108862.

[24] L. Guo, Y. Wu, F. Xu, X. Song, J. Ye, P. Duan, Z. Zhang, Sulfate resistance of hybrid fiber reinforced metakaolin geopolymer composites, Composites

Part B: Engineering 183 (2020) 107689.
[25] Y. Wang, Y. Cao, Z. Zhang, J. Huang, P. Zhang, Y. Ma, H. Wang, Study of acidic degradation of alkali-activated materials using synthetic C-(N)-A-S-H and N-A-S-H gels, Composites Part B: Engineering 230 (2022) 109510.
[26] C. Grengg, G. Koraimann, N. Ukrainczyk, O. Rudic, S. Luschnig, G. Gluth, M. Radtke, M. Dietzel, F. Mittermayr, Cu- and Zn-doped alkali activated mortar – Properties and durability in (bio)chemically aggressive wastewater environments, Cement and Concrete Research 149 (2021) 106541.
[27] F.R. Steindl, I. Galan, A. Baldermann, M. Sakoparnig, L. Briendl, J. Juhart, M. Thumann, M. Dietzel, R. Röck, W. Kusterle, F. Mittermayr, Sulfate durability and leaching behaviour of dry- and wet-mix shotcrete mixes, Cement and Concrete Research 137 (2020) 106180.
[28] T.A. Aiken, J. Kwasny, W. Sha, M.N. Soutsos, Effect of slag content and activator dosage on the resistance of fly ash geopolymer binders to sulfuric acid attack, Cement and Concrete Research 111 (2018) 23–40.
[29] T. Bakharev, Resistance of geopolymer materials to acid attack, Cement and Concrete Research 35 (2005) 658–670.
[30] S. Foorginezhad, M. Mohseni-Dargah, K. Firoozirad, V. Aryai, A. Razmjou, R. Abbassi, V. Garaniya, A. Beheshti, M. Asadnia, Recent Advances in Sensing and Assessment of Corrosion in Sewage Pipelines, Process Safety and Environmental Protection 147 (2021) 192–213.
[31] L. Biondi, M. Perry, J. McAlorum, C. Vlachakis, A. Hamilton, Geopolymer-based moisture sensors for reinforced concrete health monitoring, Sensors and Actuators B: Chemical 309 (2020) 127775.
[32] L. Biondi, M. Perry, J. McAlorum, C. Vlachakis, A. Hamilton, G. Lo, Alkali-Activated Cement Sensors for Sodium Chloride Monitoring, IEEE Sensors J. 21 (2021) 21197–21204.
[33] C. Vlachakis, M. Perry, L. Biondi, J. McAlorum, 3D printed temperature-sensing repairs for concrete structures, Additive Manufacturing 34 (2020) 101238.
[34] J. McAlorum, M. Perry, C. Vlachakis, L. Biondi, B. Lavoie, Robotic spray coating of self-sensing metakaolin geopolymer for concrete monitoring, Automation in Construction 121 (2021) 103415.
[35] M. Saafi, A. Gullane, B. Huang, H. Sadeghi, J. Ye, F. Sadeghi, Inherently multifunctional geopolymeric cementitious composite as electrical energy storage and self-sensing structural material, Composite Structures 201 (2018) 766–778.
[36] W. Dong, W. Li, N. Lu, F. Qu, K. Vessalas, D. Sheng, Piezoresistive behaviours of cement-based sensor with carbon black subjected to various temperature and water content, Composites Part B: Engineering 178 (2019) 107488.

[37] T.S. Qureshi, D.K. Panesar, Nano reinforced cement paste composite with functionalized graphene and pristine graphene nanoplatelets, Composites Part B: Engineering 197 (2020) 108063.

[38] J.-L. Le, H. Du, S.D. Pang, Use of 2D Graphene Nanoplatelets (GNP) in cement composites for structural health evaluation, Composites Part B: Engineering 67 (2014) 555–563.

[39] S. Sun, S. Ding, B. Han, S. Dong, X. Yu, D. Zhou, J. Ou, Multi-layer graphene-engineered cementitious composites with multifunctionality/intelligence, Composites Part B: Engineering 129 (2017) 221–232.

[40] O. Öztürk, G. Yıldırım, Ü.S. Keskin, H. Siad, M. Şahmaran, Nano-tailored multi-functional cementitious composites, Composites Part B: Engineering 182 (2020) 107670.

[41] Z. Tian, Y. Li, J. Zheng, S. Wang, A state-of-the-art on self-sensing concrete: Materials, fabrication and properties, Composites Part B: Engineering 177 (2019) 107437.

[42] M. Saafi, L. Tang, J. Fung, M. Rahman, F. Sillars, J. Liggat, X. Zhou, Graphene/fly ash geopolymeric composites as self-sensing structural materials, Smart Mater. Struct. 23 (2014) 65006.

[43] M. Saafi, G. Piukovics, J. Ye, Hybrid graphene/geopolymeric cement as a superionic conductor for structural health monitoring applications, Smart Mater. Struct. 25 (2016) 105018.

[44] M. Davoodabadi, I. Vareli, M. Liebscher, L. Tzounis, M. Sgarzi, A.S. Paipetis, J. Yang, G. Cuniberti, V. Mechtcherine, Thermoelectric Energy Harvesting from Single-Walled Carbon Nanotube Alkali-Activated Nanocomposites Produced from Industrial Waste Materials, Nanomaterials (Basel, Switzerland) 11 (2021).

[45] M. Davoodabadi, M. Liebscher, S. Hampel, M. Sgarzi, A.B. Rezaie, D. Wolf, G. Cuniberti, V. Mechtcherine, J. Yang, Multi-walled carbon nanotube dispersion methodologies in alkaline media and their influence on mechanical reinforcement of alkali-activated nanocomposites, Composites Part B: Engineering 209 (2021) 108559.

[46] G. Karalis, L. Tzounis, E. Dimos, C.K. Mytafides, M. Liebscher, A. Karydis-Messinis, N.E. Zafeiropoulos, A.S. Paipetis, Printed Single-Wall Carbon Nanotube-Based Joule Heating Devices Integrated as Functional Laminae in Advanced Composites, ACS applied materials & interfaces 13 (2021) 39880–39893.

[47] C.K. Mytafides, L. Tzounis, G. Karalis, P. Formanek, A.S. Paipetis, Fully printed and flexible carbon nanotube-based thermoelectric generator capable for high-temperature applications, Journal of Power Sources 507 (2021) 230323.

[48] S.I. Hwang, H.-Y. Chen, C. Fenk, M.A. Rothfuss, K.N. Bocan, N.G. Franconi, G.J. Morgan, D.L. White, S.C. Burkert, J.E. Ellis, M.L. Vinay, D.A. Rometo, D.N. Finegold, E. Sejdic, S.K. Cho, A. Star,

Breath Acetone Sensing Based on Single-Walled Carbon Nanotube-Titanium Dioxide Hybrids Enabled by a Custom-Built Dehumidifier, ACS Sens. 6 (2021) 871–880.

[49] W.-T. Koo, H.-J. Cho, D.-H. Kim, Y.H. Kim, H. Shin, R.M. Penner, I.-D. Kim, Chemiresistive Hydrogen Sensors: Fundamentals, Recent Advances, and Challenges, ACS nano 14 (2020) 14284–14322.

[50] L.A. Panes-Ruiz, M. Shaygan, Y. Fu, Y. Liu, V. Khavrus, S. Oswald, T. Gemming, L. Baraban, V. Bezugly, G. Cuniberti, Toward Highly Sensitive and Energy Efficient Ammonia Gas Detection with Modified Single-Walled Carbon Nanotubes at Room Temperature, ACS Sens. 3 (2018) 79–86.

[51] L.A. Panes-Ruiz, L. Riemenschneider, M.M. Al Chawa, M. Löffler, B. Rellinghaus, R. Tetzlaff, V. Bezugly, B. Ibarlucea, G. Cuniberti, Selective and self-validating breath-level detection of hydrogen sulfide in humid air by gold nanoparticle-functionalized nanotube arrays, Nano Res. (2021) 1–10.

[52] I. Vareli, L. Tzounis, K. Tsirka, I.E. Kavvadias, K. Tsongas, M. Liebscher, A. Elenas, L.N. Gergidis, N.-M. Barkoula, A.S. Paipetis, High-performance cement/SWCNT thermoelectric nanocomposites and a structural thermoelectric generator device towards large-scale thermal energy harvesting, J. Mater. Chem. C 9 (2021) 14421–14438.

[53] K.J.D. MacKenzie, M.J. Bolton, Electrical and mechanical properties of aluminosilicate inorganic polymer composites with carbon nanotubes, J Mater Sci 44 (2009) 2851–2857.

[54] I. Kusak, M. Lunak, On the effect of addition of carbon nanotubes on the electric conductivity of alkali-activated slag mortars, IOP Conf. Ser.: Mater. Sci. Eng. 246 (2017) 12044.

[55] M. Saafi, K. Andrew, P.L. Tang, D. McGhon, S. Taylor, M. Rahman, S. Yang, X. Zhou, Multifunctional properties of carbon nanotube/fly ash geopolymeric nanocomposites, Construction and Building Materials 49 (2013) 46–55.

[56] H. Dai, E.T. Thostenson, T. Schumacher, Comparative study of the thermoresistive behavior of carbon nanotube-based nanocomposites and multiscale hybrid composites, Composites Part B: Engineering 222 (2021) 109068.

[57] S. Lin, T.M. Swager, Carbon Nanotube Formic Acid Sensors Using a Nickel Bis(ortho-diiminosemiquinonate) Selector, ACS Sens. 3 (2018) 569–573.

[58] S. Roy, M. David-Pur, Y. Hanein, Carbon Nanotube-Based Ion Selective Sensors for Wearable Applications, ACS applied materials & interfaces 9 (2017) 35169–35177.

[59] M. He, R.G. Croy, J.M. Essigmann, T.M. Swager, Chemiresistive Carbon Nanotube Sensors for N-Nitrosodialkylamines, ACS Sens. 4 (2019) 2819–2824.

[60] S.-Y. Cho, K.M. Cho, S. Chong, K. Park, S. Kim, H. Kang, S.J. Kim, G. Kwak, J. Kim, H.-T. Jung, Rational Design of Aminopolymer for Selective Discrimination of Acidic Air Pollutants, ACS Sens. 3 (2018) 1329–1337.

[61] J.M. Casas, F. Alvarez, L. Cifuentes, Aqueous speciation of sulfuric acid–cupric sulfate solutions, Chemical Engineering Science 55 (2000) 6223–6234.

[62] M.Y. Lone, A. Kumar, S. Husain, R.C. Singh, M. Zulfequar, M. Husain, Fabrication of sensitive SWCNT sensor for trace level detection of reducing and oxidizing gases (NH3 and NO2) at room temperature, Physica E: Low-dimensional Systems and Nanostructures 108 (2019) 206–214.

[63] F. Schütt, V. Postica, R. Adelung, O. Lupan, Single and Networked ZnO-CNT Hybrid Tetrapods for Selective Room-Temperature High-Performance Ammonia Sensors, ACS applied materials & interfaces 9 (2017) 23107–23118.

[64] M. Xiao, S. Liang, J. Han, D. Zhong, J. Liu, Z. Zhang, L. Peng, Batch Fabrication of Ultrasensitive Carbon Nanotube Hydrogen Sensors with Sub-ppm Detection Limit, ACS Sens. 3 (2018) 749–756.

[65] W. Zhou, J. Vavro, N.M. Nemes, J.E. Fischer, F. Borondics, K. Kamarás, D.B. Tanner, Charge transfer and Fermi level shift in p -doped single-walled carbon nanotubes, Phys. Rev. B 71 (2005).

[66] P.J. Larkin, Illustrated IR and Raman Spectra Demonstrating Important Functional Groups, in: P. Larkin (Ed.), Infrared and Raman spectroscopy: Principles and spectral interpretation, Elsevier, Amsterdam Netherlands, Oxford United Kingdom, Cambridge MA United States, 2018, pp. 153–210.

[67] J. Coates, Interpretation of Infrared Spectra, A Practical Approach, in: R.A. Meyers (Ed.), Encyclopedia of Analytical Chemistry, Wiley, Chichester, UK, 2006.

[68] N.B. Colthup, L.H. Daly, S.E. Wiberley, CHAPTER 13 - MAJOR SPECTRA–STRUCTURE CORRELATIONS BY SPECTRAL REGIONS, in: N.B. Colthup, L.H. Daly, S.E. Wiberley (Eds.), Introduction to infrared and Raman spectroscopy, 3rd ed., Academic Press, Boston, 1990, pp. 387–481.

[69] N.B. Colthup, L.H. Daly, S.E. Wiberley, CHAPTER 8 - AROMATIC AND HETEROAROMATIC RINGS, in: N.B. Colthup, L.H. Daly, S.E. Wiberley (Eds.), Introduction to infrared and Raman spectroscopy, 3rd ed., Academic Press, Boston, 1990, pp. 261–288.

[70] I. Ismail, S.A. Bernal, J.L. Provis, R. San Nicolas, S. Hamdan, J.S. van Deventer, Modification of phase evolution in alkali-activated blast furnace slag by the incorporation of fly ash, Cement and Concrete Composites 45 (2014) 125–135.

[71] T. Bakharev, Durability of geopolymer materials in sodium and magnesium sulfate solutions, Cement and Concrete

Research 35 (2005) 1233–1246.

[72] J. Astoveza, R. Trauchessec, S. Migot-Choux, R. Soth, Y. Pontikes, Iron-rich slag addition in ternary binders of Portland cement, aluminate cement and calcium sulfate, Cement and Concrete Research 153 (2022) 106689.

[73] J. Herterich, I. Richardson, F. Moro, M. Marchi, L. Black, Microstructure and phase assemblage of low-clinker cements during the early stages of carbonation, Cement and Concrete Research 152 (2022) 106643.

[74] V. Trincal, V. Benavent, H. Lahalle, B. Balsamo, G. Samson, C. Patapy, Y. Jainin, M. Cyr, Effect of drying temperature on the properties of alkali-activated binders - Recommendations for sample preconditioning, Cement and Concrete Research 151 (2022) 106617.

[75] A.M. Efimov, V.G. Pogareva, IR absorption spectra of vitreous silica and silicate glasses: The nature of bands in the 1300 to 5000 cm−1 region, Chemical Geology 229 (2006) 198–217.

[76] T. Revathi, R. Jeyalakshmi, Fly ash–GGBS geopolymer in boron environment: A study on rheology and microstructure by ATR FT-IR and MAS NMR, Construction and Building Materials 267 (2021) 120965.

[77] Y. Liu, Raman, Mid-IR, and NIR spectroscopic study of calcium sulfates and mapping gypsum abundances in Columbus crater, Mars, Planetary and Space Science 163 (2018) 35–41.

[78] B. Huber, H. Hilbig, M.M. Mago, J.E. Drewes, E. Müller, Comparative analysis of biogenic and chemical sulfuric acid attack on hardened cement paste using laser ablation-ICP-MS, Cement and Concrete Research 87 (2016) 14–21.

[79] B. Huber, H. Hilbig, J.E. Drewes, E. Müller, Evaluation of concrete corrosion after short- and long-term exposure to chemically and microbially generated sulfuric acid, Cement and Concrete Research 94 (2017) 36–48.

[80] P. Sturm, G. Gluth, C. Jäger, H. Brouwers, H.-C. Kühne, Sulfuric acid resistance of one-part alkali-activated mortars, Cement and Concrete Research 109 (2018) 54–63.

[81] C. Grengg, G.J. Gluth, F. Mittermayr, N. Ukrainczyk, M. Bertmer, A. Guilherme Buzanich, M. Radtke, A. Leis, M. Dietzel, Deterioration mechanism of alkali-activated materials in sulfuric acid and the influence of Cu: A micro-to-nano structural, elemental and stable isotopic multi-proxy study, Cement and Concrete Research 142 (2021) 106373.

[82] A. Palomo, M.T. Blanco-Varela, M.L. Granizo, F. Puertas, T. Vazquez, M.W. Grutzeck, Chemical stability of cementitious materials based on metakaolin, Cement and Concrete Research 29 (1999) 997–1004.